Department of Astronomy
Faculty of Science
University of Helsinki, Finland

# Multiwavelength studies of regolith effects in planetary remote sensing

**Jyri Näränen**

Academic dissertation

*To be presented, with the permission of the Faculty of Science of the University of Helsinki, for public criticism in Auditorium XII on March 6, 2009, at 12 o'clock noon.*

**Cover:**
A scanning-electron-microscope image of powdered olivine basalt that has been used as an analog material for planetary regoliths in Papers I, VI, and VII of the thesis. The largest particles are a few hundred $\mu$m in diameter.

ISSN 1455-4852
ISBN 978-952-10-5284-2 (paperback)
ISBN 978-952-10-5285-9 (PDF)
http://www.ethesis.helsinki.fi
Yliopistopaino
Helsinki 2009

**Abstract**

A large proportion of our knowledge about the surfaces of atmosphereless solar-system bodies is obtained through remote-sensing measurements. The measurements can be carried out either as ground-based telescopic observations or space-based observations from orbiting spacecraft. In both cases, the measurement geometry normally varies during the observations due to the orbital motion of the target body, the spacecraft, etc.. As a result, the data are acquired over a variety of viewing and illumination angles. Surfaces of planetary bodies are usually covered with a layer of loose, broken-up rock material called the regolith whose physical properties affect the directional dependence of remote-sensed measurements. It is of utmost importance for correct interpretation of the remote-sensed data to understand the processes behind this alteration.

In the thesis, the multi-angular effects that the physical properties of the regolith have on remote-sensing measurements are studied in two regimes of electromagnetic radiation, visible to near infrared and soft X-rays. These effects are here termed generally the regolith effects in remote sensing. Although the physical mechanisms that are important in these regions are largely different, notable similarities arise in the methodology that is used in the study of the regolith effects, including the characterization of the regolith both in experimental studies and in numerical simulations. Several novel experimental setups have been constructed for the thesis. Alongside the experimental work, theoretical modelling has been carried out, and results from both approaches are presented. Modelling of the directional behaviour of light scattered from a regolith is utilized to obtain shape and spin-state information of several asteroids from telescopic observations and to assess the surface roughness and single-scattering properties of lunar maria from spacecraft observations.

One of the main conclusions is that the azimuthal direction is an important factor in detailed studies of planetary surfaces. In addition, even a single parameter, such as porosity, can alter the light scattering properties of a regolith significantly. Surface roughness of the regolith is found to alter the elemental fluorescence line ratios of a surface obtained through planetary soft X-ray spectrometry. The results presented in the thesis are among the first to report this phenomenon. Regolith effects need to be taken into account in the analysis of remote-sensed data, providing opportunities for retrieving physical parameters of the surface through inverse methods.

# Acknowledgements

I would like to show my deepest gratitude to my thesis advisor Dr. Karri Muinonen. Without his guidance and support this thesis simply would not exist. Dr. Jukka Piironen was the first to suggest all those years ago that I should go for astronomy. Apparently I have the right kind of sense of humour to be an astronomer. Dr. Sanna Kaasalainen and Dr. Jouni Peltoniemi introduced me to the world of experimental planetary research from early on. Ph. Lic. Lauri Alha taught me a lot about X-ray measurements. I'm grateful to all the contributing authors. I'm also grateful to my collegues at the Planetary research group who have all helped me in one way or another.

This work has been largely supported by funding from the Academy of Finland. Some parts of the work were done while I was employed by the Finnish Geodetic Institute. SPARTAN, an European Union funded exchange visit program at the University of Leicester Department of Physics and Astronomy, made it possible for me to spend three months at the Space Research Centre, where I learned a lot about planetary soft X-ray spectroscopy. Special thanks go to Dr. James Carpenter and Prof. George Fraser for making my visit at Leicester a success.

I would also like to express my gratitude for the Nordic Optical Telescope Scientific Association for funding my studentship at the Nordic Optical Telescope. The year I spent on La Palma was truly a magical time during which I not only learned a lot about observational astronomy but also of Life, the Universe, and Everything. I would like to thank the staff at NOT (the greatest telescope in the world!) and all the friends I made there for making the year on La Isla Bonita as one of the most memorable in my life!

I am indebted to the pre-examiners Prof. Yuriy Shkuratov and Dr. Tatsuaki Okada for their valuable comments on the thesis. I would also like to recognize the much appreciated effort of the Opponent Prof. Nicolas Thomas and that of the Custos Prof. Hannu Koskinen.

I would like to thank my parents Irmeli and Martti and my brother Marko for all the love and support I have received during all the years when I have had my head solidly above the clouds. I could not have made it without you. I also thank my friends (too many to list here but you know who you are!) for providing support and friendship that I (sometimes badly) needed. My life would be a lot emptier without you!

Special thanks go to my trusted steeds Johnson and Labadia, who have helped to keep my feet on the ground, sometimes quite literally. The long rides in the Finnish countryside during the years have been instrumental in clearing my thoughts when I have been staying behind the desk for too long.

And as I finish these thanks, the only thing I am certain of is that I have forgotten not just one important person but dozens of them. Sorry. But thank you anyway.

*Non est vivere, sed valere vita est.*

Helsinki, January 29, 2009
*Jyri Näränen*

# List of papers

I **Näränen, J.**, Kaasalainen, S., Peltoniemi, J., Heikkilä, S., Granvik, M., and Saarinen, V., 2004. Laboratory photometry of planetary regolith analogs. II. Surface roughness and extremes of packing density. *Astronomy & Astrophysics* **426**, 1103–1109.

II Peltoniemi, J. I., Piironen, J., **Näränen, J.**, Suomalainen, J., Kuittinen, R., Markelin, L., and Honkavaara, E., 2007. Bidirectional reflectance spectrometry of gravel at the Sjökulla test field. *ISPRS Journal of Photogrammetry and Remote Sensing* **62**, 434–446.

III Muinonen, K., Torppa, J., Virtanen, J., **Näränen, J.**, Niemelä, J., Granvik, M., Laakso, T., Parviainen, H., Aksnes, K., Dai, Z., Lagerkvist, C.-I., Rickman, H., Karlsson, O., Hahn, G., Michelsen, R., Grav, T., and Jørgensen, U.G., 2007. Spins, shapes, and orbits for near-Earth objects by Nordic NEON. In *Proceedings of the 236th IAU Symposium: Near Earth Objects, Our Celestial Neighbors: Opportunity and Risk* (G. P. Valsecchi and D. Vokrouhlický, Eds.), pp. 309–320, Cambridge University Press.

IV Muinonen, K., Parviainen, H., **Näränen, J.**, Josset, J.L., Beauvivre, S., Pinet, P., Chevrel, S., and Foing, B., 2008. Lunar single-scattering, porosity, and surface-roughness properties with SMART-1/AMIE, submitted to *A&A Letters*.

V **Näränen, J.**, Parviainen, H., and Muinonen, K., 2007. X-ray Fluorescence Modelling for Solar-System Regoliths: Effects of Viewing Geometry, Particle Size, and Surface Roughness. In *Proceedings of the 236th IAU Symposium: Near Earth Objects, Our Celestial Neighbors: Opportunity and Risk* (G. P. Valsecchi and D. Vokrouhlický, Eds.), pp. 243–250, Cambridge University Press.

VI **Näränen, J.**, Parviainen, H., Muinonen, K., Carpenter, J., Nygård, K., and Peura, M., 2008. Laboratory studies into the effect of regolith on planetary X-ray fluorescence spectroscopy. *Icarus* **198**, 408–419.

VII **Näränen, J.**, Carpenter, J., Parviainen, H., Muinonen, K., and Fraser, G., 2008. Regolith effects in planetary X-ray fluorescence spectroscopy: Laboratory measurements at 1.7-6.4 keV, submitted to *Advances in Space Research*.

## Acronyms used in the text

**AMIE** Advanced Moon micro-Imager Experiment

**BRF** Bidirectional reflectance factor

**BRDF** Bidirectional reflectance distribution function

**CBOE** Coherent-backscattering opposition effect

**D-CIXS** Demonstration of a Compact Imaging X-ray Spectrometer

**ESA** European Space Agency

**ESO** European Southern Observatory

**fBm** fractional Brownian motion

**FPE** Fundamental parameters equation

**IDL** Interactive Data Language

**IRAF** Image Analysis and Reduction Facility

**MC** Monte Carlo

**MIXS** Mercury Imaging X-ray Spectrometer

**NEO** Near-Earth Object

**NOT** Nordic Optical telescope

**PHO** Potentially Hazardous Object

**SHOE** Shadow-hiding opposition effect

**SEM** Scanning Electron Microscope

**SMART-1** Small Missions for Advanced Research in Technology 1

**S/N** Signal-to-noise

**SIXS** Solar Intensity X-ray and particle Spectrometer

**VNIR** Visible and near-infrared

**XRF** X-ray fluorescence

**XSM** X-ray Solar Monitor

# Contents

# 1 Introduction

The study of atmosphereless solar-system objects relies largely on remote-sensing observations from orbiting and fly-by platforms and ground-based telescopic observations that utilize different kinds of instrumentation. Ground truth is seldom available for relating the observed data to real features and materials *in situ*. The most notable exceptions are the Lunar rock material brought to Earth by the American Apollo missions and the Soviet Luna missions and also the few meteorites whose origins (the Moon, Mars, several asteroids, etc.) have been determined. The usability of these samples is limited by the way they represent their parent body. For example, the lunar samples can only represent accurately the specific location on the lunar surface, from which they have been retrieved. In the case of Martian and asteroidal meteorites, also the long travel to the Earth can have had an impact making the meteorite less representative of its origin. It is also a matter of debate how representative meteorites are of their parent body, as the parent body can have been subjected to, e.g., collisional metamorphosis and space weathering after the meteorite was formed.

Thus, in order to make full use of the remotely-sensed data, both ground-based experimental work on analog materials and numerical simulations are needed to understand the various physical processes and conditions that produce the observed signal.

## 1.1 Regolith

The word *regolith* is derived from Greek *rhegos+litho* and literally translates as blanket rock. The author who first proposed this term, Merrill (1897), coined it to describe "that great blanket of unconsolidated drift and residual material which covers the hard, rocky crust of the globe". In other words, regolith is the layer of loose, broken-up rock material that covers solid rock. Sometimes regolith is also divided into two subcategories: *soil* is the portion of regolith that has particle sizes less than 1 cm and *dust* the portion that has particle sizes less than 50 $\mu$m. In the thesis, however, no distinction is made between soil and dust.

Regolith is present on all terrestrial planets and probably on all moons and asteroids as well, at least to some extent. For those bodies, regolith constitutes a large portion of the surface that can be reached with remote-sensing methods in a wavelength region that begins from near infrared and extends all the way to X-rays. Longer and shorter waves can sometimes penetrate the surface deep enough to reach the solid rock beneath the regolith. The regolith layer has been modified over and over again by major geological processes such as impact communition, impact melting, formation of agglutinates, solar-wind sputtering, impact vaporization, impact-vapor condensation, and shock and thermal welding of grains. Thus, each regolith is unique and contains information about not only the origin of its parent body but also about its geological evolution. Regolith can be described as rough-surfaced, particulate, and porous random medium. Regolith is characterized by various physical parameters, such as *porosity*, *mean particle size* and *particle size distribution*, *particle single-scattering albedo*, *preferential orientation of particles in the medium*, and *particle shape distribution*. An additional parameter, *surface roughness* can be divided into two categories. One is the particle-scale surface roughness that is caused by the porous nature of the medium. This causes volume shadowing in visible wavelengths and also shadowing of incident and shielding of emergent X-rays. The other category of roughness is in scales larger than the particles. This causes rough-surface shadowing in visible wavelengths (e.g., Parviainen & Muinonen 2007). For more discussion about the characterization of surface roughness, see Chapt. 2 of the thesis. Porosity is defined as

$(1-\phi)$, where $\phi$ is the *filling factor* that is also called the *packing density*. Filling factor is defined by $\phi = \frac{\rho_B}{\rho_S}$ where $\rho_B$ and $\rho_S$ are the bulk density and the solid density of the sample, respectively. The effect that the change in porosity has on the surface roughness of a regolith is illustrated in Fig. 1.

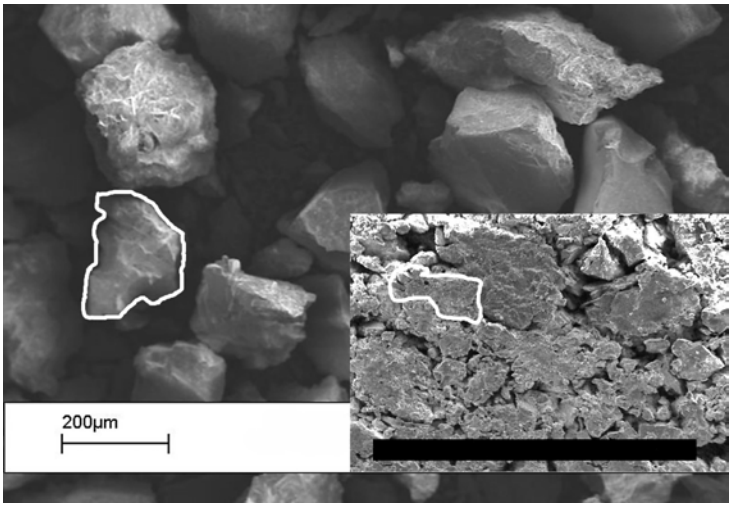


Figure 1: SEM images (Paper VII) of loose olivine basalt powder (large image) and the same powder compressed into a sample pellet (inset). The particle size range for the sample is 75-250$\mu$m, the packing density for the loose powder is $\sim$30% and for the pellet $\sim$70%. The scale bar applies to both images. A single particle is specified by white color in both images.

In addition, regolith can be characterized by several other parameters, such as its *chemical/elemental composition*, *refractive index*, and *crystalline structure*.

The physical characteristics of the regolith vary from one place to another. Understanding these physical properties can tell a lot about the environment in which the regolith was created and in which it resides. However the physical properties of the regolith itself can alter the remote sensed signal in a way that needs to be understood and taken into account when analyzing the signal. These effects vary as a function of wavelength due to, e.g., changes in fundamental physical processes when moving from one wavelength region to another.

As an example of a planetary regolith, I will discuss briefly the lunar surface. The lunar regolith is the best-studied regolith (with the exclusion of the terrestrial regolith) thanks to the samples retrieved by the Apollo (382 kg) and Luna (326 g) missions (Heiken et al. 1991). The major components in the lunar regolith are rock fragments, mineral fragments, and glassy particles that can be further divided into agglutinates, impact-glass droplets, and volcanic-glass beads. The lunar regolith particles have a mean size of $\sim 60-80$ $\mu$m and the regolith depths measured *in situ* by the Apollo missions range from two to twelve meters. The bulk density of the lunar regolith in the upper few mm is 800-1000 kg/m$^3$ and 1500-1800 kg/m$^3$ at the depth of 10-20 cm. The porosity is 35-45% at the depth of 10-20 cm. The Moon is also dramatically divided into two contrasting regions: 16% of the surface consists of dark maria and the rest 84% is lunar highlands. These two regions have different geological histories and thus different regolith properties, even on average.

As planetary regoliths are not readily available for studies conducted on Earth, the use of analog materials and simulations is necessary for work in support of the planetary studies.

For the thesis work, I have mostly used olivine basalt powder of different particle sizes

as the planetary-regolith analog material. It is considered to be a good analog material for lunar mare regolith. For more complete description of the characterization of this material, see, e.g., Papers I and VII. The original sample material has been crushed and then sieved to achieve different particle size ranges. This has, however, resulted in a nonrealistic particle size distribution within those ranges. This serves as a reminder that it is difficult to produce realistic planetary-regolith analogs. Realistic packing densities are also difficult to generate on the Earth, especially for asteroid regolith analogs. The gravity on asteroid surfaces is a few percent of the Earth's gravity and there are also other issues, such as electrostatic levitation of particles on asteroid surfaces induced by solar wind, that are almost impossible to account for.

In numerical simulations, all of the characteristics of a real regolith can be considered. However, due to limitations in computing cababilities of even the most modern computers, it is not yet feasible to include all of the characteristics of the regolith in the simulations. Some of the most common simplifications are to assume spherical particles (for media consisting of millions of such particles) or to study only individual particles with realistic shapes, etc., or clusters of such particles. In Fig. 2, a scanning-electron-microscope (SEM) image of a regolith-analog material is illustrated alongside a simulated regolith-like medium of spherical particles with a realistic particle size distribution and similar packing density.

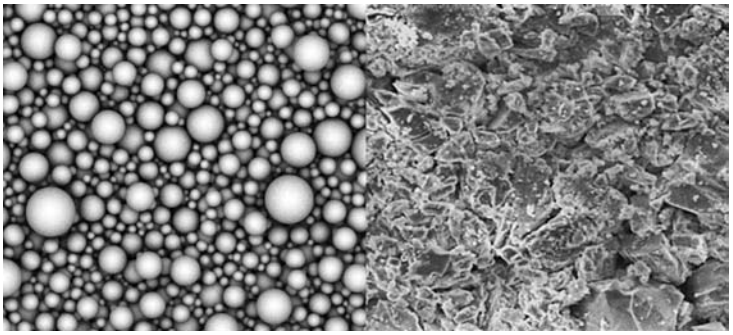

Figure 2: Simulated regolith (on the left, courtesy of Hannu Parviainen) and a SEM image of ground olivine basalt (on the right, Paper VII).

## 1.2 Direct and inverse problem

The regolith-like nature of planetary surfaces poses both difficulties and opportunities for studies that utilize remote-sensing measurements. In the former case, in order to compare data taken at different illumination and viewing angles, it is necessary to be able to remove the effects caused by the physical properties of the regolith not related to the properties under study. Thus, it needs to be understood how the physical properties of the regolith affect the measured signal as a function of, e.g., measurement geometry. This is the direct problem in planetary remote sensing. The direct problem (also known as the classical problem) deals with the problematics of how to produce results with given initial conditions. It can be formulated as:

$$\text{Model parameters} \rightarrow \text{Data}$$

Understanding and solving the direct problem helps, e.g., to restrict the free-parameter space for the inverse problem (see below) and to create better calibration methods. Often input parameters for the direct problem are obtained through meticulous experimental work in the laboratory combined with numerical simulations.

If the physical parameters of the regolith are not known, an opportunity rises to solve them through interpretation of the remote sensed data. In this case, the values of some model parameters are obtained from the observed data:

$$\text{Data} \rightarrow \text{Model parameters}$$

This is called the inverse problem. Inverse problems can be ill-posed. The attraction is, however, the additional science that can be derived from the data. Actually, most of the problems in astronomy and planetary science are inverse.

## 1.3 The aim of the thesis

The aim of the thesis has been to study the multiangular effects that the physical properties of a regolith have on remote-sensing observations of atmosphereless solar-system bodies. Several novel experimental setups have been developed to study these effects in the laboratory and in the field. Lunar and martian regolith analog materials have been utilized in laboratory studies and terrestrial regoliths in field measurements. The experimental studies are related to theoretical modelling such as that presented in Papers III, IV, and V. The effects have been studied in two different electromagnetic wavelength regions, in the visible-near-infrared wavelengths and the soft X-ray energy band.

Although the physical processes in these two wavelength regions are different, a common denominator is that the particulate and rough nature of the regolith alters the measured signal as a function of measurement geometry. Also, there is synergy in the methodology of studies of this alteration, termed "regolith effects" in Paper VI. For example, the same samples can be used in experimental studies performed in both wavelengths and, in numerical modelling, the same code can be used to create the simulated medium.

The regolith effects need to be understood and taken into account, e.g., in the calibration of remote-sensed data and in the planning of observations. The regolith effects can alter the signal measured from a regolith by tens of percents from that measured of an ideal surface. However, the alteration also presents opportunities for obtaining novel information about the physical parameters by inverse methods. Papers III and IV present such inverse studies. In Paper III, shape and spin-state of several asteroids are obtained from telescope images through inverse methods that utilize information on the multiangular scattering behaviour of asteroids. Surface roughness and packing density of lunar maria regoliths and scattering characteristics of lunar maria particles are assessed through inverse modelling of SMART-1 lunar mission data in Paper IV.

What follows is a brief overview of the peer-reviewed scientific journal and conference proceedings papers included in the thesis:

**Paper I** **Näränen J.**, Kaasalainen S., Peltoniemi J., Heikkilä S., Granvik M., and Saarinen V. 2004. Laboratory photometry of planetary regolith analogs. II. Surface roughness and extremes of packing density. *Astronomy & Astrophysics* **426**, 1103–1109.

**Paper II** Peltoniemi, J. I., Piironen, J., **Näränen, J.**, Suomalainen, J., Kuittinen, R., Markelin, L., and Honkavaara, E., 2007. Bidirectional reflectance spectrometry of gravel at the Sjökulla test field. *ISPRS Journal of Photogrammetry and Remote Sensing* **62**, 434–446.

**Paper III** Muinonen K., Torppa J., Virtanen J., **Näränen J.**, Niemelä J., Granvik M., Laakso T., Parviainen H., Aksnes K., Dai Z., Lagerkvist C.-I., Rickman H., Karlsson O., Hahn G., Michelsen R., Grav T., and Jørgensen U G 2007. Spins, shapes, and

orbits for near-Earth objects by Nordic NEON. In *Proceedings of the 236th IAU Symposium: Near Earth Objects, Our Celestial Neighbors: Opportunity and Risk* (G. P. Valsecchi and D. Vokrouhlický, Eds.), pp. 309–320, Cambridge University Press.

**Paper IV** Muinonen, K., Parviainen, H., **Näränen, J.**, Josset, J.L., Beauvivre, S., Pinet, P., Chevrel, S., and Foing, B., 2008. Lunar single-scattering, porosity, and surface-roughness properties with SMART-1/AMIE, submitted to *Astronomy & Astrophysics Letters*.

**Paper V Näränen J.**, Parviainen H., and Muinonen K. 2007, X-ray fluorescence modelling for solar-system regoliths: Effects of Viewing Geometry, Particle Size, and Surface Roughness. In *Proceedings of the 236th IAU Symposium: Near Earth Objects, Our Celestial Neighbors: Opportunity and Risk* (G. P. Valsecchi and D. Vokrouhlický, Eds.), pp. 243–250, Cambridge University Press.

**Paper VI Näränen, J.**, Parviainen, H., Muinonen, K., Carpenter, J., Nygård, K., and Peura, M. 2008. Laboratory studies into the effect of regolith on planetary X-ray fluorescence spectroscopy. *Icarus* **198**, 408–419.

**Paper VII Näränen, J.**, Carpenter, J., Parviainen, H., Muinonen, K., and Fraser, G., 2008. Regolith effects in planetary X-ray fluorescence spectroscopy: Laboratory measurements at 1.7-6.4 keV, submitted to *Advances in Space Research*.

Paper I addresses the contributions of regolith surface roughness and packing density on the opposition effect through empirical studies in the laboratory. For this study, an experimental setup was also flown on a parabolic flight to simulate microgravity environment on, e.g., the surface of asteroids. Increasing the packing density was found to increase the reflectance of the sample. The opposition peak amplitude and the width of the effect also increased. The contribution of the surface roughness at scales larger than the particles sizes, remains inconclusive.

In Paper II, the bidirectional reflectance of a terrestrial regolith measurements are reported. The paper describes the development work of spectrogoniometers (i.e., spectrometers that are attached to angle-measuring devices) at the Finnish Geodetic Institute. Such measurements are useful for both terrestrial remote sensing applications and validating modelling for planetary observations such as those described in Paper IV. The results of the paper show that the gravel samples behave as expected for particulate media. They are brightest at backscattering direction and darken monotonically toward forward direction until some forward brightening appears at phase angles ($>100°$). A further conclusion is that the difference between the reflectance of a Lambertian (diffuse) surface and a measured BRF of a regolith-like surface can be as high as 50%. In many remote-sensing applications, however, the surface is assumed as Lambertian which can introduce large errors in the analysis.

Paper III presents a study into the physical and dynamical properties of near-Earth objects (NEOs). A telescopic observation campaign was carried out at the Nordic Optical Telescope with related theoretical work. Convex inversion solutions were obtained for shapes and spin-axis orientations of three asteroids ((1685) Toro, (1981) Midas, and (1862) Apollo) and additional solutions for the possible spin and shape spaces with the novel SCyPe method (for 2002 $FF_{12}$, 2003 $MS_2$, 2003 $RX_7$, and 2004 HW).

Several properties of the lunar regolith, including single-scattering albedo, porosity, and surface roughness, are studied in Paper IV. We used broad-band visible wavelength images obtained by the ESA SMART-1 lunar mission to study the physical properties of

lunar mare regoliths. A dataset with, to my best knowledge, the largest angular range reported for space-based lunar photometric observations is presented. We put forward a conclusion that most of the lunar opposition effect is due to the coherent-backscattering mechanism with only a small contribution from the shadow-hiding mechanism. In addition, fractional-Brownian-motion (fBm) surface parameters $H = 0.4$ and $\sigma = 0.06$, as well as the packing density of 0.35, were obtained as the best fit for the surface of lunar maria.

A transition to a different wavelength/energy region is made in Paper V. In Paper V, we present a novel numerical model for studying the effects that the viewing geometry and the particle size and surface roughness of the regolith have on the observed soft X-ray fluorescence. The reduction of the particle size is found to increase the intensity of the fluorescent radiation. The effect is a function of the viewing angle. Also, an opposition effect is seen to arise at incidence angles ($\iota$) $\lesssim 10^\circ$.

A novel experimental setup has been constructed to support the numerical study presented in Paper V. We have studied experimentally how the physical properties of the regolith, in this case the particle-scale surface roughness, affect soft X-ray spectroscopy as a function of both incidence and emergence angles. This work was published in Paper VI, with a review on the previous work on the topic and discussion to place these studies in the context of planetary studies. Surface roughness is found to cause hardening (relative increase of the high-energy part of the spectrum over the low-energy part) in the spectrum as a function of the phase angle. The effect that the physical properties of the regolith, including surface roughness, have on measured soft X-ray fluorescence is termed as regolith effects in soft X-ray spectroscopy of planetary surfaces. In addition, a novel semi-empirical model is introduced for studying the regolith effects in absolute elemental line intensities.

Finally, Paper VII continues with the empirical work and presents new measurements on the regolith effects and also introduces another experimental setup. The samples are characterized more accurately than in Paper VI and the energy range under study is extended to energies as low as the Si-K$\alpha$ fluorescent line at 1.74 keV. The hardening of the spectrum as a function of surface roughness and phase angle, first published in Paper VI, is confirmed to be present at energies as low as the Si-K$\alpha$ line. A new method to separate the regolith effects and effects predicted by the fundamental parameters equation (FPE) is presented, utilizing numerical modelling of the FPE with the X-ray source spectrum.

The thesis is organized as follows. In Chapt. 2, the interactions between electromagnetic radiation and the regolith in visible and near-infrared wavelengths, that are relevant for the thesis, are described. Due to the different physical mechanisms producing soft X-ray fluorescence and monochromatic scattering in visible and near-infrared wavelengths, Chapt. 3 is dedicated to the theory of the interactions between soft X-rays and the regolith. In Chapt. 4, the different experimental setups used and observations carried out for the thesis are introduced. Summaries of Papers I-VII are given in Chapt. 5, including a brief description of my part contribution to the papers. Conclusions and future prospects are presented in Chapt. 6.

# 2 Theory for visible and near-infrared wavelengths

In this chapter and the next, some of the basic physical mechanisms involved in the interaction of electromagnetic radiation and the regolith are described. The review is limited to the wavelength region in which the experimental and observational work was carried out and to the mechanisms relevant for this thesis.

The angles used throughout the thesis are illustrated in Fig. 3. $\iota$ is the incidence angle of the radiation, $\epsilon$ is the emergence angle, $\alpha$ is the phase angle, and $\phi_0$ and $\phi$ are the azimuth angles of the incident and emergent radiation, respectively. The principal plane of radiation is defined as the normal to the surface (i.e., at $\iota = 0°$, the Sun is at zenith) and with $\Delta\phi = \phi - \phi_0 = 180°$. The angles are related to each other through the relation $\cos\alpha = \cos\epsilon\cos\iota + \sin\epsilon\sin\iota\cos\Delta\phi$.

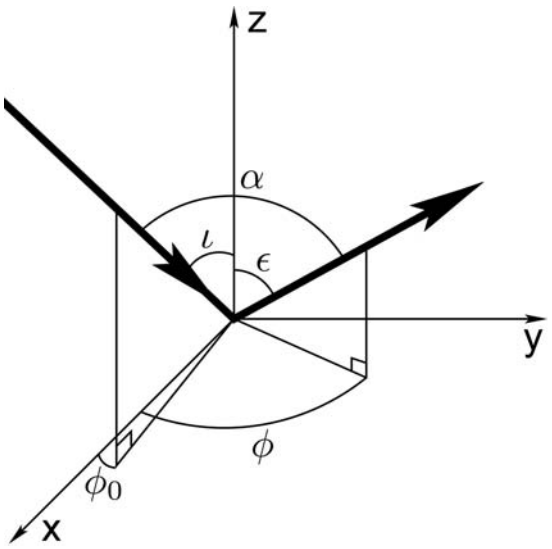


Figure 3: The observation geometry.

Visible and near-infrared wavelengths (VNIR) are defined as being approximately between 400 and 2500 nm. They cover the full visible spectrum starting from ultraviolet and also the near-infrared wavelengths up to the water absorption band at 2500 nm.

In the VNIR region, the primary interactions between electromagnetic radiation and matter are absorption and scattering. The ratio between absorption and scattering is determined by the single-scattering albedo of the particle $\tilde{\omega}$. While some absorbed radiation can be re-emitted, the effects from this are considered to be negligible and are not taken into further consideration. Also, scattering processes where the wavelength changes (i.e., inelastic scattering processes), such as Raman scattering are omitted.

Scattering can be described as a physical process in which light is forced to deviate from a straight trajectory by one or more localized non-uniformities in the medium through which it passes. When light is scattered by only one scattering center, the process is called single scattering. If the incident light is scattered by multiple scattering centers before emerging from the scattering medium, the process is called multiple scattering. Scattered light that is observed at large phase angles ($\alpha > 90°$) is called forward scattered and, respectively, scattered light that is observed at small phase angles ($\alpha < 90°$) is called backscattered.

For complete description on scattering of light, the polarization state of light should be included in addition to its intensity. However, as no studies reported in this thesis utilize polarization, polarization is largely omitted here.

For more discussion on the physics of classical electrodynamics, the reader is advised to refer to Jackson (1999). The physics of light scattering and absorption are assessed by, e.g., van de Hulst (1957), Bohren & Huffman (1998), and Hapke (1993). Here I will give a brief overview of the points of interest in the scattering theory relevant for the work included in the thesis.

Scattering from a medium can be calculated analytically in some special cases. The major scattering mechanisms for VNIR wavelengths that can be analytically solved are Mie scattering (Mie 1908) and Rayleigh scattering (Rayleigh 1871). In the former case, the scatterers are assumed to be spherical and in the latter, the scatterers are assumed to be significantly smaller than the wavelength of the incident light. Rayleigh scattering is responsible for the blue color of the sky and, for example, the ordinary rainbows can be explained by Mie scattering. For more complicated scatterers, numerical methods are often needed. Scattering from single particles with complex shapes and from clusters of such particles can be studied through numerical methods such as the well-known Discrete-Dipole Approximation (Purcell & Pennypacker 1973). However, in order to study scattering from a medium consisting of a large number of particles, simplifications often need to be used. This is to keep the number of free parameters in analytical models small enough and to keep the computation times in numerical models short enough. One often used simplification is to assume that the individual particles, from which the medium consists of, are spherical and that their surfaces follow a relatively simple scattering law, such as the Lambert's law (see below). With this simplification, the scattering can be studied, e.g., by using the geometric-optics approximation and by statistical/Monte Carlo (MC) ray-tracing computations (e.g., Stankevich et al. 2003, Shkuratov et al. 2005).

Below, I will give a brief overview of some of the most common scattering laws for planetary studies. As the field of light-scattering studies is ever expanding and evolving, I cannot hope to give an exhaustive overview. The aim is to give the reader some insight into the free-parameter space used in the study of light scattering from planetary surfaces. Here, scattering law is defined as the generic way a surface element redistributes the incoming radiation. The different types of reflectance functions associate radiometric quantities with each other according to reflectance laws.

However, before proceeding to the scattering laws, two important terms used in this thesis need to be explained: the bidirectional reflectance distribution and the opposition effect.

## 2.1 Bidirectional reflectance distribution

The intensity and spectral distribution of light scattered from a regolith is strongly dependent on the direction of target illumination and observation. This dependence on the two directions is described using a bidirectional reflectance distribution function (BRDF) or bidirectional reflectance factor (BRF).

A sample surface can scatter radiation into different directions, with the intensity varying with changes in both the incidence and emergence angles. BRDF is the function that describes this reflectance characteristic for all the relevant angles. In practice, the complete BRDF is difficult to measure. Instead, the BRF is commonly used as it can be directly measured. The BRF is defined in terms of the ratio of the radiance reflected by a target surface, $L_{target}$, into a specific viewing angle, $(\epsilon, \phi)$, and the radiance reflected in the same direction by a Lambertian surface (see below) at the same location, $L_{\mathrm{Lambert}}$. BRF is described by Glickman (2000):

$$\mathrm{BRF}\left(\iota, \phi_0, \epsilon, \phi\right) = \frac{\mathrm{L_{target}}\left(\epsilon, \phi, \iota, \phi_0\right)}{\mathrm{L_{Lambert}}\left(\epsilon, \phi, \iota, \phi_0\right)} \tag{1}$$

The radiant flux incident on the surface is from a well-collimated beam (such as direct sunlight) with a known illumination direction, $(\iota, \phi_0)$, as shown in Fig. 3. BRF is unitless. Fig. 4 illustrates measured BRF for a terrestrial regolith, black gabbro.

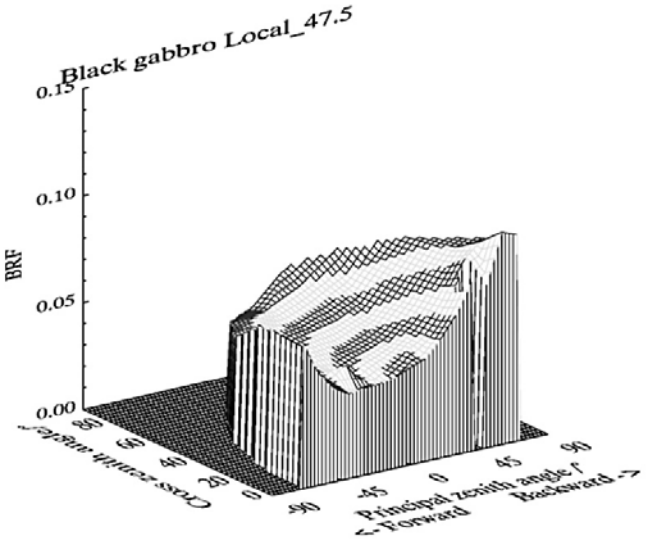


Figure 4: An example of BRF measured in Paper II. The sample is terrestrial regolith, black gabbro gravel. Incidence angle is 47° and wavelength $560 \pm 10$ nm.

BRF is directly related to the BRDF by:

$$\mathrm{BRF}\,(\iota, \phi_0, \epsilon, \phi) = \pi \cdot \mathrm{BRDF}\,(\iota, \phi_0, \epsilon, \phi) \tag{2}$$

BRDF can also be defined as the ratio of the reflected intensity $I(\mu, \phi)$ to the incident unidirectional flux $F_0(\mu_0, \phi_o)$ (Peltoniemi et al. 2005a), where $\mu = \cos\epsilon$ and $\mu_0 = \cos\iota$:

$$R(\mu, \mu_0, \phi, \phi_0) = \frac{I(\mu, \phi)}{\phi_0 F_0(\mu_0, \phi_0)} \tag{3}$$

## 2.2 Photometric opposition effect

At small phase angles ($\alpha \lesssim 10°$), almost all atmosphereless solar-system bodies exhibit an anomalous nonlinear increase in the measured brightness. This phenomenon is called the photometric opposition effect (Gehrels 1956) and is illustrated in Fig. 5 for martian-regolith analog material measured in Paper I. The opposition effect of the Moon is particularly interesting because it is easily observable with bare eyes. On the night of the opposition (or on the nights when the Moon is closest to the opposition as complete opposition implies lunar eclipse) the Moon is roughly twice as bright as on the nights just before or after the opposition. Around opposition, the surface features of the Moon also seem to disappear due to the lack of shadows. The opposition effect was first observed in the rings of Saturn, where it is particularly evident, by Seeliger in the late 19th century. He also proposed that a shadow-hiding mechanism is responsible for the observed increase in brightness. The shadow-hiding opposition effect (SHOE) is discussed in, e.g., Lumme & Bowell (1981*a*) and Hapke (1986).

The shadow-hiding opposition effect arises from the fact that a ray of light penetrating into the scattering medium and incident on a certain particle can always emerge back along the path of incidence whereas, in other directions, the emerging ray can be blocked by other particles. Shadow-hiding is inherently a first-order multiple-scattering mechanism. Shadow-hiding can be divided into two different mechanisms: internal shadow-hiding

that depends mainly on the packing density (or porosity) of the scattering medium and interfacial shadow-hiding that depends mainly on surface roughness. Shadow-hiding can be largely addressed by the geometric-optics approximation.

Particles and surface features on particles that have a size parameter $X = \frac{2\pi r}{\lambda} \lesssim 1$ do not have well-defined shadows, thus SHOE is not expected to play a major part in scattering on a medium consisting of such particles. However, when $X \sim 1$ an entirely different phenomenon can cause a surge in brightness at small phase angles. The phenomenon is known as the coherent backscattering or weak photon localization (e.g., Kuga & Ishimaru 1984, Shkuratov 1988, Muinonen 1990, Hapke 1990).

Coherent backscattering opposition effect (CBOE) can be qualitatively explained by the fact that two partial waves associated with the same wave front may travel the same multiply scattered path between particles of the medium, but in opposite directions. At zero phase angle, or if the separation of the entrance and exit points of the partial waves is small, the waves are in phase with each other and constructive interference occurs. Otherwise they interfere randomly. CBOE has been suggested as one of the causes of the strong opposition surges (an additional increase in the opposition effect at phase angles smaller than few degrees) of icy satellites and asteroids and as a contributor to the lunar opposition effect in Paper IV.

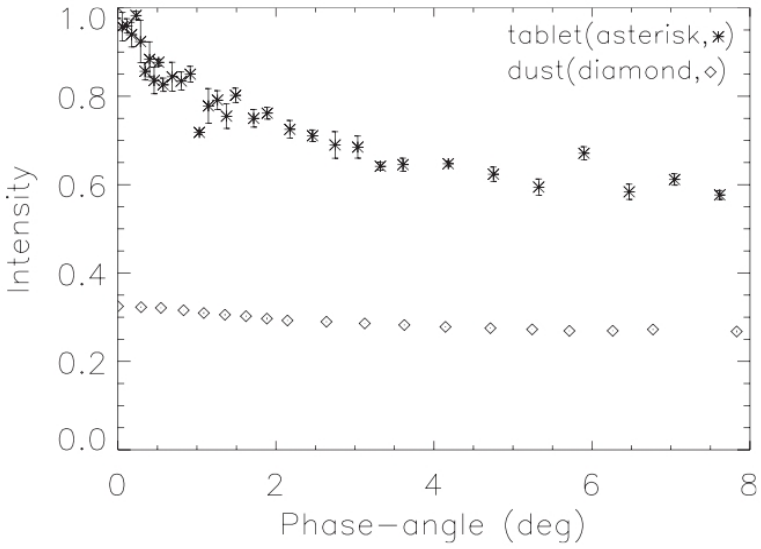


Figure 5: The photometric opposition effect measured of a martian-regolith analog material (oxidized basalt with particle sizes $< 75$ $\mu$m) in Paper I. The figure shows also the effect of compaction on the reflected brightness of the material. The intensity values are normalized to the highest value at 0° phase angle. The diamonds represent uncompressed powder and the asterisks a compressed pellet.

The effects that the roughness and packing density of the regolith have on the opposition effect are studied experimentally in Paper I.

## 2.3 Lambert and Lommel-Seeliger scattering laws

In planetary astronomy, light scattering from regoliths is commonly approximated by Lambert and Lommel-Seeliger reflection laws. Lambert's law is simply a cosine law describing isotropic reflection, i.e., the incident radiation is reflected uniformly to all directions. This is considered to be a valid first-order approximation for objects with relatively

high albedos. The radiance of such a surface is simply

$$L_L \sim F\mu_0, \tag{4}$$

where $F$ is the incident radiant flux density, and $\mu_0 = \cos\iota$. However, if one considers a planetary object, such as the Moon, it becomes obvious that the Lambert law is incorrect. If the Moon were a Lambertian surface, substantial darkening would be observed near the terminator (large $\iota$).

The Lommel-Seeliger law is based on the theory of radiative transfer. It is a single-scattering model that is derived, e.g., in Fairbairn (2005) and the derivation is not reproduced here. Radiance given by the Lommel-Seeliger law is, assuming isotropic single scatterin,

$$L_{LS} = \frac{\tilde{\omega_0} F}{4\pi\mu} \frac{\mu_0\mu}{\mu + \mu_0}, \tag{5}$$

where $\mu = \cos\epsilon$. The Lommel-Seeliger law describes fairly well scattering from rough and especially dark-albedo objects. It does not, however, display an opposition effect (see Sect. 2.2).

These two scattering laws can be combined to form a one-parameter scattering model that is simple enough for fast computation and describes the scattering characteristics of atmosphereles solar-system bodies reasonably well. It is of use especially in applications where parameters other than the scattering model are assumed to produce larger errors. This is the approach used in Paper III for the shape and spin-vector computations. In the general form, the scattering model can be formulated as

$$S(\mu, \mu_0) = \frac{\mu\mu_0}{\mu + \mu_0} + c\mu\mu_0 \tag{6}$$

where $c$ is a weight factor for the Lambertian part. By selecting different weights, the albedo of the object can be taken into account: the higher albedo the object has, the more weight is put on the Lambertian part.

While the Lambert and Lommel-Seeliger laws work well as a first-order approximation for reflectance of diffuse surfaces, they are still far from describing reflectance of realistic rough surfaces, such as planetary regoliths. Neither of the models take into account, e.g., self-shadowing of particles in a particulate medium. For this reason, more advanced analytical models have been developed.

## 2.4 Hapke scattering law

Among the most frequently used scattering laws based on radiative transfer is the so-called Hapke's law. It was first presented by Hapke (1981) and several modifications to it have been presented since then, adding, e.g., the treatment for the coherent backscattering (see Sect. 2.2). The rough-surface part of the Hapke's law assumes that the surface statistics are Gaussian with isotropic distribution in azimuth.

The latest version of the law can be found in Hapke (2008). The BRDF derived in that paper for equant particles is

$$r(\iota, \epsilon, \alpha) = K \frac{\tilde{\omega}}{4\pi} \frac{\mu_0}{\mu_0 + \mu} H(\mu_0)\, H(\mu), \tag{7}$$

where

$$K = -\ln\left(\frac{1 - 1.209\,\phi^{2/3}}{1.209\,\phi^{2/3}}\right), \tag{8}$$

$$H(x) = \frac{1 + \frac{2x}{K}}{1 + \frac{2\sqrt{1-\tilde{\omega}}x}{K}}, \tag{9}$$

and $\phi$ is the packing density. The latest version of Hapke's law takes also into account the porosity of the medium and the results from this law agree qualitatively well with, e.g., the empirical results presented in Paper I.

Hapke's law has, however, received criticism due to the large number of free parameters that result sometimes in unambiguous results and nonphysical values for the parameters obtained from the best fits to data (e.g., Piironen 1998). The unambiquity in the results can also be related to the somewhat simplistic treatment of surface topography in Hapke's law (Shkuratov et al. 2005).

## 2.5 Lumme-Bowell scattering law

Another popular scattering law based on the radiative-transfer theory is the Lumme-Bowell scattering law that was first presented in Lumme & Bowell (1981*a*). The law was subsequently used by Lumme & Bowell (1981*b*) for asteroid photometry, and by Lumme & Irvine (1982) for lunar photometry. In the Lumme-Bowell law, the phase curves of atmosphereless solar-system objects can be generated from a single phase function by varying a parameter they termed the multiple-scattering factor, $Q$, which is a result of two parameters that decribe the structure of the particulate surface layer: roughness and porosity. In the general form, the law gives the normalized integrated brightness

$$\Phi_{\rm obs}(\alpha) = \frac{L(\alpha)}{L(0^\circ)}, \tag{10}$$

where $L(0^\circ)$ is the brightness at zero phase angle and $L(\alpha)$ the brightness at phase angle $\alpha$. Then, the integrated brightness is

$$\Phi_{\rm obs}(\alpha) = (1 - Q)\Phi_1(\alpha) + Q\Phi_M(\alpha), \tag{11}$$

where $Q$ is now defined as $L_M(0^\circ)/L(0^\circ)$, that is, the ratio of the multiply scattered intensity to the total intensity at zero phase angle. $\Phi_1$ and $\Phi_M$ stand for the theoretical normalized brightness due to single and multiple scattering. They may be written as

$$\Phi_1 = \Phi_P(\alpha, g)\, \Phi_R(\alpha, \rho)\, \Phi_S(\alpha, D) \tag{12}$$

and

$$\Phi_M \approx \frac{[\sin\alpha + (\pi + a)\cos\alpha]}{\pi}, \tag{13}$$

where Eq. 13 is approximated by the phase function for a Lambertian sphere. $\Phi_P$ represents the phase function for a single surface particle, $\Phi_R$ accounts for surface roughness, and $\Phi_S$ accounts for the particulate nature of the surface layer including mutual shadowing (i.e., SHOE). In Eq. 12, $g$ is the Heneye-Greenstein (e.g., van de Hulst 1970) asymmetry factor, $\rho$ is the roughness parameter defined as the ratio of the depth to the radius of a surface irregularity, and $D$ is the volume (packing) density of the surface layer. More complete derivation of the Lumme-Bowell law can be found in Lumme & Bowell (1981*a*).

The Lumme-Bowell scattering law is also used as the basis for the $H, G$ system for asteroid phase-curve (the observed magnitude behaviour as a function of phase angle) interpretation that was accepted by the International Astronomical Union Commission 20 as the standard system for the expression of asteroid phase curves. Although the Lumme-Bowell law fits the phase curves of asteroids well, it does not take into account, e.g., coherent backscattering. This results sometimes in less-than-optimal fits, especially, for brighter objects.

## 2.6 Scattering model of Paper IV

In Paper IV, a new approach for modelling the reflectance of particulate surfaces by utilizing numerical methods is presented. The BRDF of the regolith is first modelled by generating a medium of spherical particles with a realistic size distribution and packing density. The surface of the medium is bound by a two-dimensional random fBm field (Parviainen & Muinonen 2007), a fractal surface. The roughness of the fBm field is described by two parameters: the Hurst exponent $H$ and standard deviation of heights $\sigma$. A Lommel-Seeliger reflectance model with an isotropic phase function is selected as BRDF of the surfaces of scattering elements (single particles). Monte-Carlo (MC) ray-tracing is then used to compute the BRDF from the simulated medium. The computed BRDF takes into account the mutual shadowing between regolith particles in scales large compared to the wavelength of the incident light ($\mathrm{SM_p}$, shadowing mechanism of porous medium) and shadowing caused by the rough interface between free space and regolith ($\mathrm{SM_r}$, shadowing mechanism of rough surface). The BRDF also takes into account the azimuthal dependence of shadowing. Several BRDFs are created within the free-parameter space considered realistic. The best-fitting BRDF to the observational data can then be found using MC minimization methods, and subsequently reduced from the data, resulting in a so-called volume-element scattering phase function (VSPF) that describes the scattering properties of large particles composed of the inhomogeneous structures and/or smaller particles in a submicron-to-micron scale. The best fit also provides estimates for $H$ and $\sigma$ of the observed surface. Once the shadowing effects have been taken into account, a more elaborate multiple-scattering modelling is utilized to assess single scattering and coherent-backscattering (see Sect. 2.2) properties of the VSPF. This way, for example, the scattering behaviour at phase angles smaller than $10^\circ$ can be explained satisfactorily.

# 3 Theory for soft X-rays

The soft X-ray region is located between the regions of extreme ultaviolet and hard X-rays. In planetary astronomy, the soft X-ray energy range is normally considered to lay between approximately 0.5 and 10 keV, i.e., ∼2.5 and 0.12 nm. I will follow the convention to use energy, instead of wavelength, to characterize the X-ray radiation. In this Chapter, I will give an overview on the basic concepts and processes of X-ray physics relevant to this thesis and also explain the basic theory of X-ray fluorescence spectroscopy from orbiting platforms and the regolith effects that are introduced in Papers V, VI, and VII. Although particle processes, such as particle-induced X-ray emission (PIXE), are important for planetary X-ray spectroscopy, they have not been included in our studies and their theoretical treatment is omitted here.

## 3.1 X-ray fluorescence

Below about 10 keV, the dominant interaction between an incident photon (X-ray) and matter is photoelectric absorption. An electron can be ejected from its atomic orbital (shell) by the absorption of an X-ray of sufficient energy. The energy of the X-ray ($h\nu$) must be greater than the energy with which the electron is bound to the atom.

When an inner-shell electron is ejected from an atom, an electron from a higher-energy-level shell will be transferred to the lower-energy-level shell. During this transition, an X-ray is emitted that has the energy equal to the potential difference between the two shells. This X-ray can either excite further Auger electron emission from outer shells or it can escape from the atom producing X-ray emission.

This fluorescent emission is called the characteristic X-ray emission of the element, or secondary radiation. Fluorescent X-rays are labelled according to the shell from which they originate from (K, L, M, etc.) and to the number of shells above that, from which the decaying electron originated (denoted as $\alpha$ for one, $\beta$ for two, etc.). For example, Ca K$\alpha$ fluorescent X-ray originates from the transfer of an electron from the L-shell to the K-shell in the calcium atom after an electron has been removed from the K-shell through photoabsorption.

The probability for the production of a fluorescent X-ray in the event of absorption is given by a statistical parameter called the fluorescent yield $\omega_i$ ($i$ denoting the shell whence the emission is excited from). The energy of the emitted X-ray is equal to the difference in energies between the two shells occupied by the electron making the transition. Because the energy difference between two specific atomic shells, in a given element, is always the same (i.e., characteristic of a particular element), the X-ray emitted when an electron moves between these two levels, will always have the same energy. Therefore, by determining the energy of the X-rays emitted by a particular element, it is possible to determine the identity of that element. The fluorescent X-rays have equal probability to be emitted in every direction regardless of the direction of the radiation that has produced it, i.e., X-ray fluorescence is an isotropic process.

For a particular energy of fluorescent X-rays emitted by an element, the number of X-rays per unit time (generally referred to as peak intensity or count rate) is related to the amount of that analyte in the sample. The counting rates for all detectable elements within a sample are usually calculated by counting (integrating), for a set amount of time, the number of photons that are detected for the various analytes' characteristic X-ray energy lines. It is important to note that these fluorescent lines are actually observed as peaks with a semi-Gaussian distribution because of the imperfect resolution of detectors. Therefore, by determining the energy of the X-ray peaks in a sample's spectrum, and

by calculating the count rate of the various elemental peaks, it is possible to qualitatively derive the elemental composition of the samples and to quantitatively measure the concentration of these elements.

The derivation of the relationship between the incident radiation and the measured fluorescent X-rays is complex and the details can be found in many books, such as those by Jenkins et al. (1981) and by Tertian & Claisse (1982). The treatment here follows that given in Van Grieken & Markowicz (2002). The intensity of the fluorescent radiation, $I_i(E_i)$ of element $i$ in a completely homogeneous sample of thickness $l$ (cm) excited by continuum radiation is described by

$$I_i(E_i)\ \mathrm{d}\Omega_\iota\ \mathrm{d}\Omega_\epsilon = \frac{\mathrm{d}\Omega_\iota\ \mathrm{d}\Omega_\epsilon}{4\pi\ \sin\iota} \int_{E_{c,i}}^{E_{max}} a_i(E_0) \frac{1 - e^{-\rho l(\mu(E_0)\csc\iota + \mu(E_i)\csc\epsilon)}}{\mu(E_0)\csc\iota + \mu(E_i)\csc\epsilon} I_0(E_0)\,\mathrm{d}E_0 \qquad (14)$$

where

$$a_i(E_0) = W_i \tau'_i(E_0) \omega_i p_i \left(1 - \frac{1}{j_i}\right) \qquad (15)$$

and $\mathrm{d}\Omega_\iota$ and $\mathrm{d}\Omega_\epsilon$ are the differential solid angles for the incident and emerging radiation, respectively, $E_{c,i}$ and $E_{max}$ are the critical absorption energy of element $i$ and the maximum energy in the excitation spectrum, $\rho$ is the density of the sample (g/cm$^3$), $\mu(E_0)$ and $\mu(E_i)$ are the total mass attenuation coefficients (in cm$^2$/g) for the whole sample at energies $E_0$ and $E_i$, respectively, $I_0(E_0)\,\mathrm{d}E_0$ is the number of incident X-rays per second per steradian in the energy interval $E_0$ to $E_0 + \mathrm{d}E_0$, $W_i$ is the weight fraction of the $i$th element in the sample material, and $\tau'_i(E_0)$ is the total photoelectric mass absorption coefficient for the $i$th element at the energy $E_0$ (in cm$^2$/g). $j_i$ is the ″jump ratio″, a constant by which the photoelectric absorption cross sections are obtained in multiple-absorption-edge region. Basically, it is $\tau$ just above an absorption edge divided by $\tau$ just below that absorption edge. A useful approximation for the calculation of the jump ratio for the K-shell is given by Poehn et al. (1985)

$$j_K = 1.754 \times 10 - 6.608 \times 10^{-1} Z + 1.427 \times 10^{-2} Z^2 - 1.1 \times 10^{-4} Z^3 \qquad (16)$$

for elements $11 \leq Z \leq 50$.

In Eq. (14), the contribution of the effective area (efficiency) of the detector at given energies is omitted as it can often be directly calibrated from the spectra before further analysis. If need be, it can be included in the formulation as a weighting factor. Eq. (14) is one form of the so-called fundamental parameters equation (FPE) of X-ray fluorescence. Other derivations of FPE relevant for planetary science can also be found in, e.g., Paper VII, Carpenter (2006), and Clark & Trombka (1997).

The mass attenuation coefficient of the whole sample $\mu$ can be approximately evaluated from the mass attenuation coefficients of the constituent elements, $\mu_i$, according to the weighted average:

$$\mu = \sum_{i=1}^{n} W_i \mu_i, \qquad (17)$$

where $W_i$ is the weight fraction of the $i$th element and $n$ is the total number of the elements in the absorber. This treatment does not take into account the changes in the atomic wave function resulting from changes in the molecular, chemical, or crystalline environment of an atom.

As the solid angles $\Omega_\iota$ and $\Omega_\iota$ are normally large in an experiment, Eq. (14) should also be integrated over these finite solid angles. However, such calculations can often be omitted and for a given measurement geometry an experimentally determined geometry

factor $G$ can be applied. If the excitation source is monochromatic (such as the Fe 55 radioactive source used in Paper VII), Eq. (14) simplifies to

$$I_i(E_i) = G\,\frac{a_i(E_0)\,I_0(E_0)}{\sin\iota}\,\frac{1-e^{-\rho\,l(\mu(E_0)\,\csc\iota+\mu(E_i)\,\csc\epsilon)}}{\mu(E_0)\csc\iota+\mu(E_i)\csc\epsilon} \tag{18}$$

Equations (14) and (18) do not take into account the secondary and higher orders of fluorescence, i.e., fluorescence excited by fluorescent X-rays of higher energies that are absorbed before exiting the medium. This is an important contributor to the observed fluorescent X-ray spectrum as some of the high-energy fluorescent X-rays produce fluorescent X-rays of lower energies. Thus, the shape of the fluorescent spectrum is changed. To take higher orders of fluorescence into account, in the case of monochromatic X-ray excitation, a factor $1+H_i$ should be included in Eq. (18), where $H_i$ is the enhancement term defined as (Shiraiwa & Fujino 1966)

$$\begin{aligned} H_i = \frac{1}{2\mu_i(E_0)}\sum_{k=1}^{m} W_k\,\omega_k\,\left(1-\frac{1}{j_k}\right)\,\mu_i(E_k)\,\mu_k(E_0) \\ \times\left(\frac{ln\left(1+\frac{\mu(E_0)}{\mu(E_k)\sin\iota}\right)}{\frac{\mu(E_0)}{\sin\iota}}+\frac{ln\left(1+\frac{\mu(E_i)}{\mu(E_k)\sin\epsilon}\right)}{\frac{\mu(E_i)}{\sin\epsilon}}\right). \end{aligned} \tag{19}$$

For continuum (and combination) X-ray sources, the analytical treatment becomes increasingly more difficult. On the other hand, using a numerical Monte-Carlo ray-tracing approach, such as that started in Paper V, the increased complexity and orders of fluorescence only increase the computation time. It should be underscored at this point that the treatment above assumes a perfectly homogeneous and plane-parallel medium. Some insight into how the inclusion of the physical parameters of the regolith affect the fluorescent spectrum is given below in Sect. 3.4 and is also the topic of Papers V, VI, and VII.

## 3.2 X-ray scattering

There are several processes in which X-rays can also be scattered when interacting with matter. For energies above ∼10 keV, the dominant interaction for X-rays with matter is Compton scattering. In Compton scattering, the X-ray interacts with an atomic electron. The X-ray is scattered from the electron with changed direction and energy, i.e., energy is transferred into the electron. For this reason, Compton scattering is called inelastic (incoherent) scattering. For energies below 10 keV, however, the contribution of inelastic scattering to the overall interactions between radiation and matter is very small.

Some of the incident X-rays are also scattered elastically (i.e., with no energy loss) from bound electrons in the atoms. In this case, the atom is neither ionized nor excited. This elastic scattering is sometimes called coherent scattering or Rayleigh scattering (not to be mixed with Rayleigh scattering in the visible wavelengths).

A useful simple criterion for judging the angular spread of the elastic scattering is given by Van Grieken & Markowicz (2002):

$$\theta_e = 2\arcsin\left(\frac{0.0133Z^{1/3}}{E(\mathrm{MeV})}\right), \tag{20}$$

where $\theta_e$ is the opening half-angle of a cone containing at least 75% of the elastically scattered radiation. This implies, that for the low Z elements from which regolith mostly

consists of and for soft X-ray energies, elastic scattering can be considered as an isotropic process. The efficiency of elastic scattering is only a few percent of that of the photoabsorption in soft X-ray energies and materials of regolith-like composition.

## 3.3 X-ray fluorescence studies in planetary science

X-ray fluorescence spectrometers are standard instruments in the typical suite used to study atmosphereless planetary bodies in the inner solar system from orbiting platforms. X-ray spectrometers are also used in planetary landers but, as those measurements are different in nature from those on orbiting platforms, I will omit them from discussion here. As the primary source for X-rays that excite fluorescence in the solar system is the solar corona, which for the most time (energetic flares being the exception) is a relatively weak source of X-rays, these studies are limited to the innermost ∼3 AU of the Solar System. However, several very interesting planetary bodies can be accessed by this technique, including Mercury, the Moon, and near-Earth objects. During a flare, the Solar X-ray flux over the energy of 1-10 keV can vary 3-4 orders of magnitude in time scales of less than one hour. During a flare, the spectral shape of the Solar X-ray spectrum also changes, with increased amount of radiation in the high-energy end of the spectrum (i.e., the spectrum hardens). As the X-ray fluorescence is highly dependent on the shape of the spectrum of the exciting source, a way to monitor the incident Solar X-ray spectrum is needed alongside the primary measurements. One way is to include a dedicated X-ray Solar monitor, such as XSM on SMART-1 (Huovelin et al. 2002). The other way is to include a Solar-pointing calibration sample that is measured by a dedicated channel of the primary instrument (Okada et al. 2006).

The first X-ray spectrometers carried to an orbit around another planetary body were those onboard the Apollo 15 and 16 missions (Adler et al. 1972). Since the Apollo days, the spatial and spectral resolution, and the overall sensitivity available for space-based X-ray instruments, have improved substantially. XRFSs have been included in the payloads of several orbiting planetary spacecraft. The past missions include: NEAR Shoemaker mission to asteroid (433) Eros (Goldsten et al. 1997) and SMART-1 mission to the Moon (Grande et al. 2003). The Hayabusa probe (Okada et al. 2006) is currently returning to the Earth after orbiting asteroid (25143) Itokawa. Kaguya, Chang'E-1, and Chandrayaan-1 are orbiting the Moon (Okada et al. 2002, Huixian et al. 2005, Joy et al. 2008). MESSENGER is currently enroute to Mercury and will arrive in March 2011 (Schlemm et al. 2007). X-ray fluorescence spectrometers will also be included in the payloads of future missions such as the European mission to Mercury, BepiColombo (launch in 2014, Schulz & Benkhoff 2006).

Soft X-ray fluorescence spectroscopy provides elemental abundance maps of major rock-forming elements, such as aluminium, magnesium, silicon, calcium, titanium, and iron in the topmost layer (∼10-100 $\mu$m) of the regoliths on the surfaces of planets and small bodies in the inner solar system (Adler & Trombka 1970). These elemental abundance maps are invaluable for the geochemical study of the surface. They provide information about a planet's surface geology which can in turn be used to infer the planet's crustal evolution. Crustal evolution can have further implications for investigations into the bulk composition of a planet, therefor placing important constraints on its origin and evolution (Rothery et al. 2008). The planet/asteroid-meteorite connection can also be studied through X-ray fluorescence spectroscopy (Nittler et al. 2004, Arai et al. 2008).

As an example of a result from planetary soft X-ray fluorescence measurement, a map of aluminium-silicon ratios as measured by Apollo 15 and 16 is shown in Fig. 6. The Al/Si ratio is lowest over the mare regions such as Mare Crisium, Mare Serenitatis, and Mare

Tranquillitatis. The Al/Si ratio is about a factor of two higher over non-mare regions, such as the semicircular arc of highlands south of Mare Crisium. Aluminum is particularly abundant in the mineral plagioclase, which is a common constituent of rocks in highland regions on the Moon. The combination of low aluminum abundance in the mare, together with the high iron abundance in these regions measured by the Gamma-ray Spectrometer, is evidence that the mare are generally composed of basalt, even in regions that were not directly sampled by the Apollo missions.

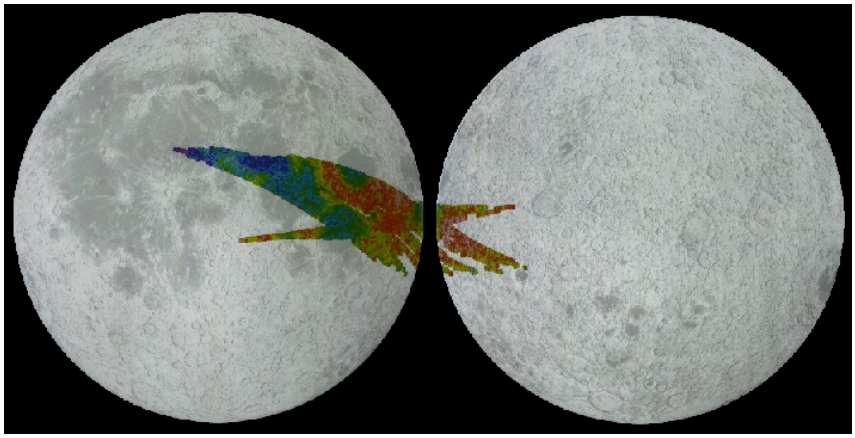

Figure 6: Al/Si elemental ratios on the Moon measured with Apollo 15 and 16 missions. Red and blue imply high and low ratios, respectively. As the lunar silicon abundance measured by these missions is relatively constant, this map depicts effectively the aluminium abundance. Picture courtesy of NASA.

## 3.4 Regolith effects

Historically, the analyses of planetary soft X-ray data from orbiting platforms have utilized fluorescence modelling based on FPE (cf. Eq. 14). In such analyses, the surface has been assumed to be plane-parallel and homogeneous. Considering how complex a technique the soft X-ray fluorescence spectroscopy is and the relatively low signal-to-noise ratio of the observations as well as the poor spatial and spectral resolution obtainable with the instruments that have flown this far, this is a reasonable simplification. The limitations on the quality of the analyses have come not from the fluorescence modelling but from other sources. However, the situation is improving with new detector technologies being introduced for space missions as discussed above. Thus, also the fluorescence modelling will need to be improved.

As shown in Chapt. 2, the interactions of photons with the regolith, as opposed to an ideal surface, result in large effects in the visible-wavelength spectroscopy and photometry. These effects are related to characteristic parameters of the regolith, such as particle size distribution, packing density, and surface roughness. In Paper VI, a review is given on the work that has been done to study the effects the physical properties of the regolith have on multiangular soft X-ray spectrometry, or the regolith effects as we have termed them. I will give here a qualitative overview of the regolith effects and the mechanisms causing them.

Fig. 7 shows the basic interaction of an X-ray with regolith. As the mean free paths of soft X-rays in a medium of planetary regolith-like chemical composition are of the order of tens to a few hundreds of $\mu$m, the single particles can be approximated to be spherical in the first instance (the mean particle size in planetary regoliths is from several tens of $\mu$m to about a hundred $\mu$m). The most notable effects caused by the regolith are

the shadowing of the incident X-rays and shielding of fluorescent X-rays (e.g., Paper VI, Maruyama et al. 2008) caused by the porosity and surface roughness of the medium. In the following, the X-ray source is considered to be a stable continuum source.

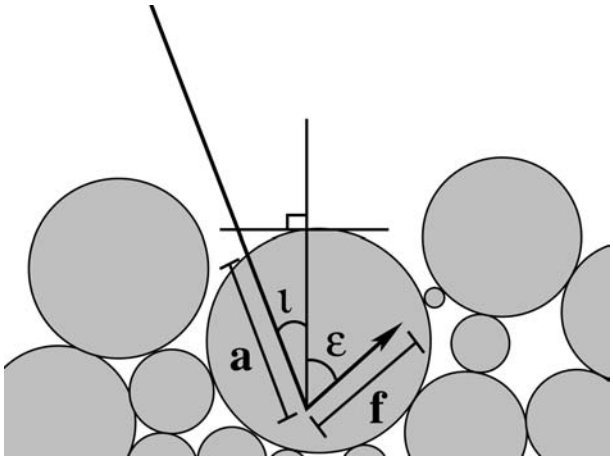


Figure 7: An illustration of the regolith effect. $a$ is the mean free path of the incident radiation before absoption and $f$ is the mean free path of the fluorescent X-rays. Note also, that $a$ is always longer than $f$ for any realistic planetary soft X-ray fluorescence scenario.

Qualitatively, shadowing means that, as the incidence angle increases (large $\iota$), the exciting radiation has an increasing chance to enter the sample medium through the side of a particle, a pore, or a roughness feature. The fluorescent X-rays excited by this radiation have to travel longer inside the medium to be observed by a detector than do X-rays excited by radiation that entered the medium at a point closer to the topmost level of the interface between the regolith and free space. As the mean-free paths of soft X-rays in a regolith-like medium increase as a function of the energy of the X-ray, the fluorescent X-rays of higher energies can escape the medium more freely than those with lower energies. This introduces a hardening (i.e., a relative enhancement of the high-energy part of the spectrum over the low-energy part) of the spectrum as a function of the incidence angle. Shielding, on the other hand, can be explained by the fact that as the emergence angle increases, the fluorescent X-rays, in a particulate medium, have statistically larger possibility of interacting with another particle, and potentially being absorbed, before vacating the medium. This is demonstrated for visible wavelength rays in Parviainen & Muinonen (2007), and a similar kind of shadowing function is also utilized in Paper V. The shadowing-induced hardening is demonstrated in Fig. 8 for the Fe-K$\alpha$/Ca-K$\alpha$ relative elemental line intensity ratio measured at different incident angles. The figure is from Paper VII, where regolith effects are measured using two experimental setups.

In addition to the surface-roughness effects, several studies (Paper V, see also references in Paper VI) have shown the existence of a particle size effect. In summary, the total fluorescent intensity of a particulate medium depends on the particle sizes in the medium. In a medium with regolith-type chemical composition, the smaller the particles are the higher the total fluorescent intensity. This effect is energy dependent. As the particle size distribution of the medium is correlated with its porosity and also with surface roughness, this effect cannot be considered entirely independent from the surface-roughness effect.

In Paper VI, an example is given on the importance of understanding the regolith effects. The NEAR-Shoemaker mission to asteroid (433) Eros carried onboard an X-ray spectrometer (XRS, Evans et al. 2001) that measured the relative elemental fluorescent line ratios of several important rock-forming elements. These ratios were compared to

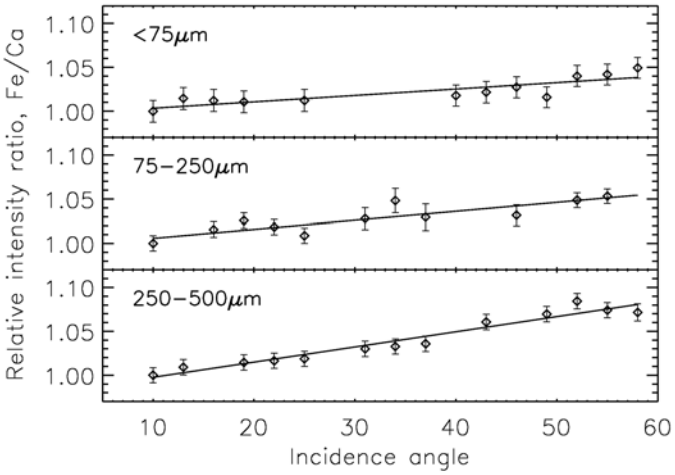


Figure 8: The Fe-K$\alpha$/Ca-K$\alpha$ line ratio measured at different angles of incidence from olivine basalt samples of three different particle-size distributions (Paper VII). The ratio increases (spectrum hardens) as a function of incidence angle. The increase is largest for the sample with the largest particle sizes that is considered to have the roughest surface.

similar ratios obtained from several meteorite types in order to establish a connection between the asteroid and meteorite types. The closest correlation was obtained with H -chondritic meteorite. However, an independent instrument, the Gamma-ray spectrometer, pointed towards a lower iron content L or even LL -chondrites. Okada (2004) was the first to point out that during its measurements of the asteroid, the spacecraft phase angle was always $\sim 90^\circ$. He then proposed that the regolith effects would have hardened the soft X-ray fluorescent spectrum, essentially increasing the derived iron content. If regolith effects are accounted for in the analysis, correlation with L or LL -chondrites would become a possibility also for the XRS data (see Fig. 9). However, other possible sources for the mismatch between the results from different instruments were proposed already by Nittler et al. (2001). More work, both theoretical and numerical (such as that started in Papers V, VI, and VII), is needed to understand the regolith effects quantitatively.

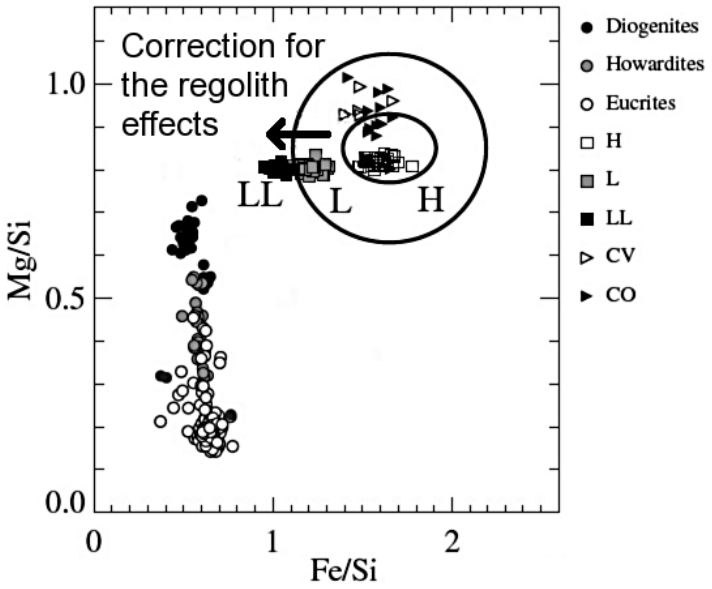


Figure 9: An example on how the correction for regolith effects will influence the establishment of the asteroid-meteorite connection. The example is an adaptation from the paper by Nittler et al. (2001) on the results from NEAR-Shoemaker that orbited the asteroid (433) Eros. The smaller ellipse represents two times the standard error of the mean and the larger error ellipse indicates the $2\sigma$ variability in the data. The ellipses would be moved to the left and a bit higher if corrections for regolith effects would be made, as discussed in Paper VI. The phase angle was $\sim 90^\circ$ for these observations.

# 4 Experiments and observations

Many laboratory and field experimental setups for simulating the interaction of electromagnetic radiation with the regolith have been created over the years. These experiments, while highly valuable as independent studies, are also invaluable for validating theoretical research. For example, the experiments described in Sects. 4.1.1 and 4.1.2 can be used to validate conclusions from numerical methods, such as the novel treatment of the lunar photometric data presented in Paper IV and also described in Chapt. 2. The work presented in Papers VI and VII have also the provision of reference data as one of their main aims.

In order to be useful for theoretical studies and to provide unambiguous interpretation of the results, the characterization of the sample material is of utmost importance. The physical parameters that can be used to describe the regolith should be quantified. This is not always easy and is often not given enough emphasis by authors presenting their experimental results. In addition, the key founding stone of science is reproducibility. To this end, the experimental setup itself should be described in as much detail as possible so that the reader can understand the process that led to the results of the study.

In the Chapter, I will introduce the different experimental setups that have been used in the thesis. More detailed descriptions can be found in Papers I, II, VI, and VII. I will also describe the observations that were used in Papers III and IV.

## 4.1 Visible and near-infrared wavelengths

The interaction of light and regolith at VNIR wavelengths can be measured via a multitude of different methods. In the present thesis, two experimental setups are used: visible-near infrared (VNIR) spectroscoscopy using a continuum light source (either an artificial one or the Sun) and laboratory photometry using a monochromatic light source, i.e., laser. Both setups are goniometric, i.e., they are capable of measuring the angles relevant to the measurements. For the spectroscopic studies the whole hemisphere above the sample was measured to obtain the BRF of the sample. For the photometric studies, which concentrated on the opposition effect, only the principal plane was measured and at relatively small phase angles. In addition to these laboratory measurements, two remote-sensing methods were used in this thesis: telescopic observations of asteroids and photometry of the lunar surface with the AMIE camera onboard the ESA SMART-1 mission.

### 4.1.1 Small-phase-angle measurements

The photometric studies presented in Paper I concentrated on measuring scattered intensity at relatively small phase angles, i.e., smaller than 10°. In order to reach the exact zero phase angle, an innovative experiment setup was constructed at the University of Helsinki Department of Astronomy (Kaasalainen et al. 2002) and later also at the Finnish Geodetic Institute. Reaching very small phase angles is in most goniometric setups not possible due to the fact that, in the zero-phase-angle geometry, either the detector moves in front of the light source or vice versa. One way to solve this problem is to use a beamsplitter (a partly-transmitting partly-reflecting optical component) as illustrated in Fig. 10. The light traverses from the light source to the beamsplitter, where part of the beam is reflected to the sample and part is transmitted through to a beam dump. Then, part of the light scattered from the sample traverses through the beamsplitter to the detector and part back to the direction of the light source. The phase angle can be changed by rotating the beamsplitter. The other more commonly used way to reach small phase angles is to increase the distances of the detector and the light source from the sample. As examples

of goniometers utilizing such an approach the University of Kharkov ($\alpha = 0.2 - 17°$) and JPL ($\alpha = 0.05 - 5°$) goniometers should be mentioned (Ovcharenko et al. 2006). As was discussed in Sect. 2.2, this is the phase-angle region where the opposition effect is at its largest.

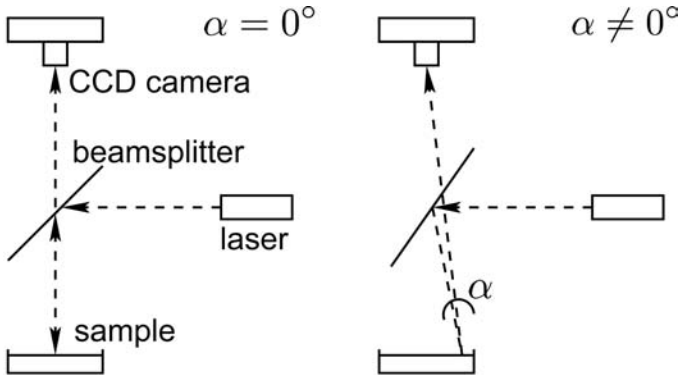


Figure 10: The experimental setup used for small-phase-angle measurements.

The greatest disadvantage of a setup utilizing beamsplitters is the limited phase-angle coverage, i.e., very large phase angles cannot be reached. For example, the experimental setup used in this thesis could only reach ∼20 degrees. At larger phase angles, the beamsplitter starts to behave in a nonlinear manner (i.e., 50/50% transmittance/reflectance ratio is not quaranteed). Also, the detector field of view is of concern. The detector used in this setup is a CCD camera. The smaller the detector angular reach is (i.e., more pixels/angular unit), the higher the angular resolution that can be achieved. However, for the specific purpose of studying the very small phase angles, this setup is very efficient. The exact zero phase angle can be reached and the angular resolution is very high, usually better than 0.1°.

Both HeNe and diode lasers were used as light sources in this study. Laser is easily collimated (the light pattern is uniform) and a relatively stable light source. Its drawbacks include the inherent possibility of speckles (bright constructive interference patterns) as well as its monochromaticity which makes broadband studies impossible. Also, the absolute polarimetric characteristics of the laser are not easily controlled without a controlled laboratory environment and, therefore, no polarimetric studies are reported here. For more detailed discussion on the experiment setup, see, e.g., Paper I, Kaasalainen (2002), and Kaasalainen et al. (2003). For discussion on the use of a broadband-spectrum light source, see Kaasalainen et al. (2005).

**Scattering@Zero-g**

In order to study the opposition effect of a medium with very low packing density (high porosity), an experimental setup similar to the one used in the laboratory was proposed to fly with the European Space Agency (ESA) parabolic flight program as a part of an ESA student outreach project. The proposal was accepted with the experimental team consisting of the author along with three co-investigators. Major modifications were made to the experimental setup to comply with the extensive security requirements of the parabolic flights. The flight campaign took place in July 2003 in Bordeaux, France. Whereas the results were not conclusive due to technical difficulties that resulted in a premature termination of the second flight of the campaign and thus reduced the number of datapoints by ∼30%, they serve as a demonstration for the experimental technique and were published as part of Paper I.

### Spectralon

The measurements at small phase angles as well as at larger phase angles as described in Sect. 4.1.2 were all calibrated or normalized using a white reference material called *Spectralon* (Courréges-Lacoste et al. 2003). Spectralon is a very good approximation of a Lambertian diffusely scattering surface and is a widely-accepted white reference standard. It is made of thermoplastic resin that gives the highest diffuse reflectance of any known material or coating over the UV-VNIR region. In the context of the studies presented in the thesis, Spectralon is mostly assumed to be a perfect Lambertian surface, although it is known to show some forward-scattering enhancement at very large scattering angles and also a small opposition effect.

## 4.1.2 Spectrogoniometric measurements

Whereas traditional goniometers cannot reach very small phase angles, they can measure the reflectance of a sample over large phase-angle ranges and also at different azimuths thus providing measured bidirectional reflectance factors (BRFs) of the targets. BRF relates the reflectance from a target surface to a white (Lambertian) standard, such as Spectralon (see above).

### Spectrogoniometers at the Finnish Geodetic Institute

Spectrogoniometer is a term coined for an instrument that consists of a spectrometer that is attached to a device capable of measuring some or all of the angles relevant to the measurement, i.e., angles of incidence, emergence, and the azimuthal angles, to a high precision. The use of a high-resolution spectrometer as the detector allows for studies on the wavelength dependence of reflectance. However, a drawback is that imaging capability does not exist and, thus, the measured spectrum is an integrated average over the footprint of the detector field-of-view on the sample surface.

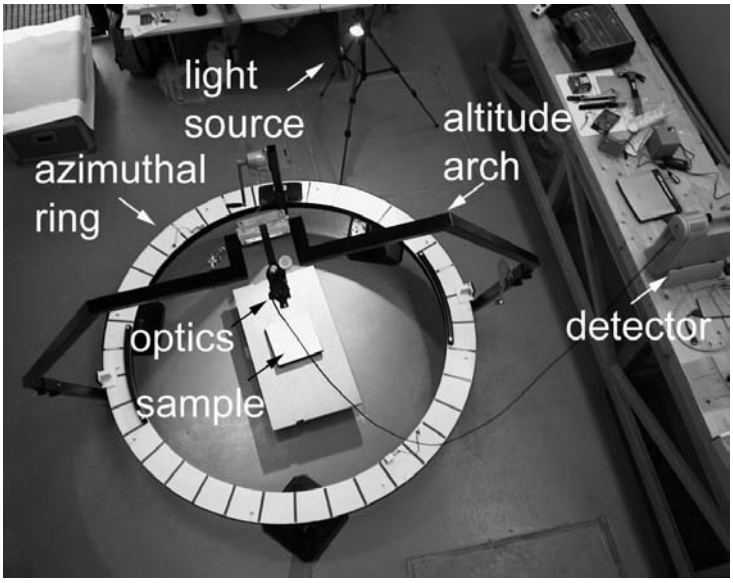


Figure 11: An illustration of the Model 3 spectrogoniometer at the Finnish Geodetic Institute. Image by the Author.

I have participated in developing and using several spectrogoniometers at the Finnish Geodetic Institute (FGI). The spectrogoniometer that I have been mostly using is called Model 3 (see Fig. 11). Model 3 consists of a horizontally mounted ring that can be

rotated in azimuth direction and of an arch mounted on the azimuth ring that can be lowered from nadir-looking point down to about 70° zenith distance. The fore-optics of the detector are located at the top of the arch. The spectrometer used with Model 3 is ASD Field Spec Pro FR, which can measure spectra in the wavelength range of 350-2500 nm, with spectral resolution of 10 nm. The signal is fed to the spectrometer through an optical fiber from the fore-optics. The footprint of the field-of-view of the detector on the target depends on the fore-optics used. Usually, a 3° fore-optics has been used resulting in a footprint of ∼10 cm in diameter on the target. The main advantage of Model 3 over many other spectrogoniometers is that it can be used for field work, i.e., measuring land and vegetation samples *in situ* without having to disturb them by transporting them into a laboratory. This is accomplished by its very robust structure and simplicity of design. Also, no electrical parts are used for the goniometer, i.e., it is fully manual to operate. Model 3 has also been used for laboratory work.

For day-time *in situ* mesurements, the Sun has been used as the light source. In night-time and in laboratory measurements, an artificial Oriel 1000 W QTH light source is used. A large benefit of performing the measurements in a laboratory is that the direction of the light source can be regulated. For calibration of the diffuse background light and the light-source stability, a Spectralon white-reference plate was also measured and, subsequently, the spectra were normalized to it to obtain the BRF.

The development of goniometers at FGI has continued over the years and some of the work that has been done is reviewed in Paper II. Also, more detailed discussion on the measurements is included in Paper II. Model 3 and the models prior and after it (at the moment, the latest version is Model 6) have also been used to study lots of other surfaces including, e.g., snow (Peltoniemi et al. 2002, Peltoniemi et al. 2005a) and understory vegetation in a pine forest (Peltoniemi et al. 2005b).

### 4.1.3 Telescopic observations

The observations reported in Paper III were, for the most part, performed at the Nordic Optical Telescope (NOT) in support of the Nordic Near-Earth-Object Network (Nordic NEON) that started its operations in 2004. The main objective of the Nordic NEON is to improve the understanding of the physical and dynamical properties of Near-Earth Objects (NEOs) by performing selected observations and contributing to the theoretical work in this field of research.

NOT is a 2.56-m telescope located at La Palma on the Canary Islands (see Fig. 12. For the observations reported here, we used the Andalucia Faint Object Spectrograph and Camera (ALFOSC) instrument that is a $2 \times 2$ kilopixel CCD camera that has an effective field-of-view of about $6' \times 6'$. Bessell R filter was used for the observations of the asteroids, since the camera is highly efficient in that channel and the asteroids are mostly at their brightest at those wavelengths. In addition, $2 \times 2$ binning of the images was used to increase the signal-to-noise ratio and to reduce the readout times of the detector.

We performed two modes of observations. The first observations were aimed at providing photometric data for shape and spin-state characterization of the targets. Although some of the observations were performed at photometric nights (no clouds and seeing remained relatively stable) and suitable photometric standard stars were measured, no absolute photometry is used for results in Paper III. This is mainly due to the fact that relative photometry is sufficient for the spin-state and shape analysis introduced in Paper III. For efficient use of the telescope time, we developed an observational strategy where several asteroids were observed simultaneously, with the telescope rotated from one target to another between the exposures (during readout). This way we obtained $\sim$ 30%

Figure 12: The Nordic Optical Telescope is located at the Roque de Los Muchachos Observatory (La Palma, Canary Islands). At the altitude of 2382 m from the sea level the observing conditions are among the best in the world. Image by the Author.

more data points per target asteroid per night without any significant loss of temporal resolution.

In addition to the photometric observations, astrometric observations were carried out. Most of these observations were performed during service observation nights at the NOT and thus the observations had to be constrained to a time frame of two hours. We developed an optimal observation strategy also for the astrometric targets. In this strategy, the same target was imaged two to four times in three sets (in total 6-12 images per target), the amount of images depending on the expected S/N ratio (more images for the poorer S/N). About 8 targets were selected for one observation run so that the time slot could be filled completely. We also placed special emphasis on obtaining as large a time separation as possible between the first and last image of each target to provide astrometric analysis using as long a time arc as possible. For the fastest moving targets, we utilized differential tracking of the telescope, i.e., the tracking of the telescope was offset by the estimated speed of the asteroid. In this mode, the exposure times could be made longer since the target remained a point source instead of a trail. The difficulty in this type of observations lies in obtaining accurate astrometric solution for the position of the target (the background is blurred by the differential tracking). The Nordic NEON program and its first results are discussed to more detail in Paper III.

Telescopic observations are often restrained by the instrumentational capabilities of the telescope and the light-gathering power of the telescope and the instrument. However, similar to laboratory work, with careful planning of the observations, the scientific output of an observation campaign can be increased considerably.

### 4.1.4 Space-based photometry

In contrast to the telescopic observations of solar-system objects that are limited in their spatial resolution and angular range, space missions can provide very-high-resolution data over large angular ranges. In Paper IV, new photometric observations of the Moon are presented. These observations were performed with the AMIE micro-imaging camera (Muinonen et al. 2002) onboard the ESA SMART-1 mission to the Moon (Fig. 13 and Pinet et al. 2005). AMIE was a compact $1024 \times 1024$ pixel CCD camera with 8 filters permanently attached in front of the field-of-view of the camera. Six of the filters were

used for push-broom type multicolour photometric imaging, one for a laser-link telecommunication experiment, and one was a pancromatic (i.e., clear) channel with the largest field of view. The latter was used in the study presented in Paper IV.

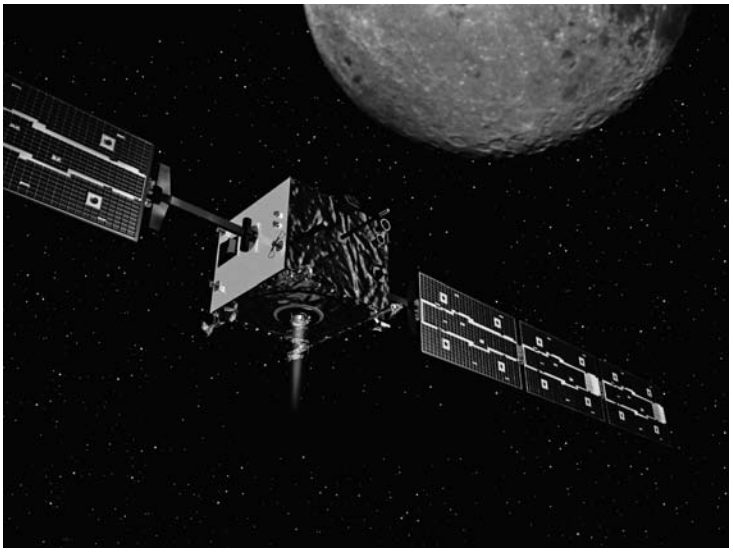

Figure 13: SMART-1 spacecraft was the first ESA mission to the Moon. During its orbital mission lasting 22 months it imaged the Moon in visible wavelengths and mapped the mineralogy of the lunar surface in infrared wavelengths. It also carried an X-ray spectrometer. Image courtesy of ESA.

AMIE imaged the Moon over 200 000 times during the SMART-1 orbital mission. Special emphasis was placed on imaging the polar regions in search of peaks of permanent light and craters of permanent darkness that are important for future manned space missions to the Moon. However, other locations were also extensively imaged. Off-nadir pointing imaging was performed on selected locations. This allowed a large phase-angle range to be covered. For our study, we selected 220 images of four lunar mare regions. The images were selected to exclude any notable albedo features and craters in order to provide the photometric analysis using as homogeneous data as possible. The datapoints within the images were hand-selected to remove albedo anomalies as much as possible. However, some differences between images of similar terrain types such as reported in Kreslavsky et al. (2000) may remain a factor. In this image set, the spatial resolution of the images varies from 288 m/pixel to 29 m/pixel. The angular ranges are: $\iota = 7 - 87°$, $\epsilon = 0 - 53°$, and $\alpha = 0 - 109°$. This presents, to my best knowledge, the largest angular coverage in any lunar photometric data set from an orbiting platform.

We utilized NASA/NAIF SPICE routines (Acton 1999) to calculate accurate positions for each pixel in the image, thus providing high-accuracy angular resolution to the data. In addition to emergence, incidence, and phase angles, also the azimuthal direction in the observations was calculated for each datapoint. This is an important new free parameter for the modelling of the photometric data, as discussed in Sect. 2.6. In effect, we measured the BRF of a surface of another planetary body.

## 4.2 X-ray fluorescence measurements

Soft X-ray goniometric (i.e., multiangular) spectroscopy, such as that reported in Papers VI and VII, is an ongoing research effort in support of the Mercury Imaging X-ray Spectrometer (MIXS) onboard BepiColombo, a ESA/JAXA spacecraft to study Mercury (due for launch in 2014). The research concentrates in studying the difficulties and prospects

that multiangular X-ray spectrometry in the backward direction (as dictated by the illumination geometries available for orbiting spacecraft) can offer when the spatial and spectral resolution of the instrument is improved and the particulate nature of the regolith is taken into account.

The importance of X-ray spectrometry in planetary research was already discussed in Sect.3.3. Here I will introduce the experimental setups that were used to study, especially, the effects that the physical properties of the regolith have on the analysis of the X-ray fluorescence measurements.

Whereas experimental and observational work in VNIR wavelengths is nontrivial, several additional challenges are introduced when measuring fluorescent emission in the soft X-ray energy band. In this energy band, air at NTP (normal temperature and pressure) conditions is very efficient in absorbing and scattering radiation. This necessitates the use of either vacuum chambers or chambers filled with neutral gas (e.g., Helium) in experimental setups that measure X-ray fluorescence. As fluorescence is an energy-dependent process, the use of spectrometers is needed for efficient measurements. Imaging X-ray spectrometers were not available for studies conducted for this thesis. As the X-rays are invisible to human eyes, there follows an additional source for uncertainty that needs to be accounted for: extra care has to be taken to ensure the pointing of the incident X-ray radiation as well as the detector field-of-view. Also, any sources for X-rays in the background need to be eliminated as such X-rays cannot be distinguished from the fluorescent X-rays from the sample.

The setup that was used for the experimental work was originally designed for the scientific ground calibration of the X-ray Solar Monitor (XSM) (Huovelin et al. 2002) of the SMART-1 lunar probe. The setup is located at the Division of Materials Physics at the University-of-Helsinki Department of Physics and is depicted in Fig. 14. The setup, hereafter referred to as Setup A, consists of a cylindrical chamber which can be pumped into near vacuum (4 mbar) to reduce the effects (absorption, scattering) of air on the measured signal. The sample in Setup A is fixed in a vertical position. This and the use

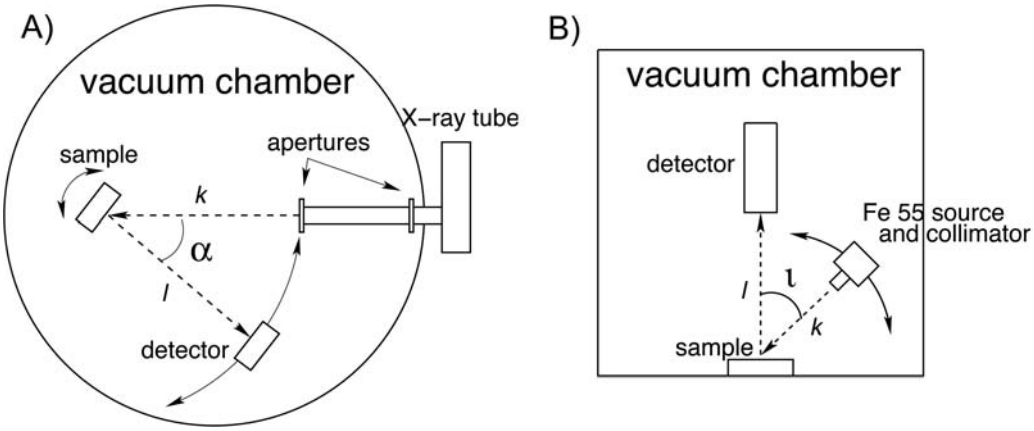


Figure 14: The experimental setups used for the goniometric X-ray measurements. The view is from the top, i.e., the setups are horizontal. Setup A is the one located at the Department of Physics, University of Helsinki, and Setup B is the Martian Environment Simulator at the Space Research Centre, University of Leicester. A phase-angle range of $\sim 7-51^\circ$ can be obtained with Setup A by either fixing the sample surface normal to the direction of the X-ray beam or to the direction of the detector boresight. In Setup B, the sample is fixed with its surface normal pointing towards the detector and incidence-angle range obtainable is $\sim 25-70^\circ$. The image is from Paper VII.

of vacuum necessitates the particulate sample to be pressed into pellets. Scanning-electron

microscope images and computer-tomography (CT) scans of the pellets were obtained for surface characterization (Fig. 15). The sample can either be fixed to the direction of the light source or it can be rotated with the detector so that the sample-detector angle is fixed. The rotation is achieved with a stepper motor that is controlled via the same computer interface as the detector. The phase-angle $\alpha$ range reachable with this setup is $\sim 7-51°$, limited by the movement range of the detector inside the chamber. The detector used for Setup A is a laboratory replica of the XSM. It has a field of view of about 90° and spectral resolution of $\sim$ 350 keV at 6.4 keV. The X-ray source is a Ti-anode X-ray tube that produces a Bremsstrahlung spectrum superposed with Ti-K$\alpha$ and $\beta$ fluorescent lines. The incident beam is collimated by two adjustable slits at the ends of a tube. A relatively small beam width of $\sim 0.2°$ on the sample surface can be obtained without increasing the integration time excessively. Several elemental fluorescent lines are measurable with this setup from a sample with regolith-type elemental composition. These include the K, Ca, Mn, and Fe K emission lines. Ti-K emission lines would be measurable if it were not for the strong backscattered radiation from the X-ray source.

Additional laboratory measurements were performed at the Space Research Centre, University of Leicester, with the Martian Environment Simulator (MES). The MES is essentially a vacuum chamber that houses an X-ray detector that can be adapted for various purposes, such as the goniometric measurements presented in Paper VII. The layout of the experiment is illustrated in Fig. 14. Only nadir-pointing geometry ($\epsilon = 0°$) is allowed for. The sample is vertical and thus pellets were used also with Setup B. The incidence angle was changed manually by moving the location of the X-ray source inside the vacuum chamber. The incidence-angle $\iota$ range obtainable with this setup is $\sim 25-70°$. A radioactive Fe 55 source was used as the X-ray source. It emits only characteristic Mn-K$\alpha$ (5.90 keV) and K$\beta$ (5.89 keV) line radiation and is thus easily modelled. However, a radioactive source is relatively weak as the source for fluorescence excitation and thus a collimation of the beam to a large full-width at half-maximum of $\sim$ 10° had to be allowed for. The collimated beam intensity profile is triangular. This may smear some of the angle-dependent effects. The detector is Amptek XR-100CR with an average energy resolution obtained in our measurements of 260 eV at 4.5 keV and 320 eV at 6 keV. The vacuum ($\sim 5{\cdot}10^{-4}$ mbar) provided the possibility of observing fluorescent emission lines down to the Si-K$\alpha$ at 1.74 keV. Also, the fluorescent Ti-K lines were available for this setup as is not the case with the Setup A.

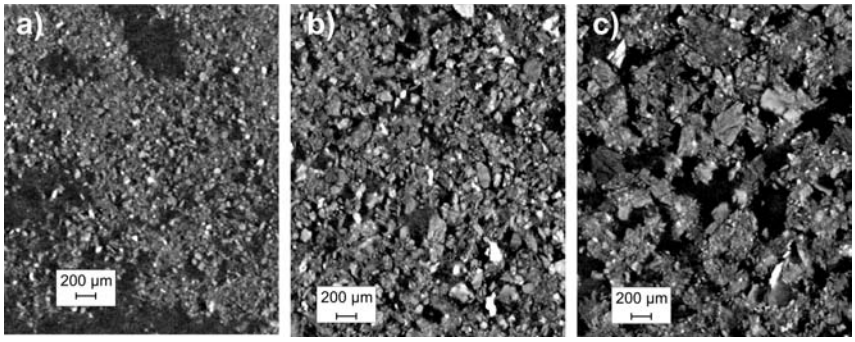


Figure 15: Two-dimensional slices of CT-scan images (Paper VII) of the sample pellets at a depth of $5 - 10\,\mu$m from the sample surface. The sample with smallest particles is labeled $a$, medium-particle-sized sample is labeled $b$, and the sample with largest particles is labeled $c$.

For the interpretation of the results, especially, the angular behaviour of the absolute line intensities, it is important to recall that, in both of the experimental setups, the

detector field-of-view is considerably larger than the X-ray source footprint on the sample surface. Thus, the X-ray source beam width produces a limitation to the angular resolution of the measurement (i.e., the larger the beamwidth, the larger angular range the detector measures).

# 5 Summary of papers

In the Chapter, I give an overview of the scientific papers that are included as part of the thesis. I also explain briefly my contribution to these papers.

## 5.1 Paper I

**Laboratory photometry of planetary regolith analogs. II. Surface roughness and extremes of packing density.** The paper is a continuation of a previous laboratory study of the opposition effect (Kaasalainen 2003). The laboratory setup used in this study was explained in more detail in Sect. 4.1. The innovation behind this kind of a setup is the use of a beamsplitter to reach the zero phase angle at an angular resolution of 0.1° or better. For this paper, the setup was also adapted to and flown on an ESA parabolic flight campaign. During the parabolic flight, microgravity environment is achieved which we used to study backscattering from a very loose dust sample: to my best knowledge, these are the first measurements of their kind. The same sample material was subsequently studied in normal gravity conditions as loose powder and as compacted pellets. Thus, three different packing conditions were achieved for the sample. In addition to packing density, the contribution of surface roughness on the observed opposition effect was studied qualitatively. Two sample materials were used, olivine basalt (a lunar mare regolith analog) and oxidized basalt (an analog material for dark martian terrains). Increasing packing density was found to increase the reflectance of the sample. This is in accordance with, e.g., a later study by Hapke (2008). The opposition peak amplitude and the width of the effect are also increased. The contribution of the surface roughness, at least on the scales used in this study, remains inconclusive.

## 5.2 Paper II

**Bidirectional reflectance spectrometry of gravel at the Sjökulla test field.** In this paper we report bidirectional reflectance measurements of terrestrial regoliths, namely the Sjökulla test site for aerial imaging. The site consists of four types of gravel in two sizes (diameters 8-26 mm and 4-8 mm). In addition, the use of spectrogoniometers for BRF measurements is discussed as well as the importance of BRF measurements for realistic radiometric calibration of remote-sensing instruments. The different target materials show distinctive BRF patterns underlining the importance of understanding not only the reflectance behaviour of a regolith material in the principal plane but also in the whole hemisphere created by introducing also the azimuth angles to the observations. Results of the paper show that the gravel samples behave as expected for particulate media. They are brightest at the backscattering direction and darken monotonically toward forward direction until some forward brightening appears at phase angles (>100°). For the BRF, the shape is strongly bowl-like for the dark samples and almost flat for the bright ones. All of the features of the BRF are enhanced at large solar zenith angles. A further conclusion is that the difference between the reflectance of a Lambertian (diffuse) surface and a measured BRF of a regolith-like surface can be as high as 50% at a given wavelenght and angle. In many remote-sensing applications, however, the surface is assumed as Lambertian which can introduce large errors in the analysis.

## 5.3 Paper III

**Spins, shapes, and orbits for near-Earth objects by Nordic NEON.** A Nordic observing program for NEOs is presented in this paper. A summary of all the observa-

tions between June 2004 and September 2006 is given. The objectives of the program are twofold: astrometric observations are performed to recover and follow-up faint potentially hazardous objects (PHOs) and photometric observations are performed to better the physical understanding (in this instant, of their shapes and directions of spin vectors) of PHOs and other NEOs. To this end, novel theoretical methods are also developed. For astrometry, three statistical inversion methods for orbit computation have been used: the nonlinear least-squares method with linearized covariances (LSL), the Volume-of-Variation method (VoV), and orbital ranging (see references for all of the methods in the Paper). The highlights of the astrometry work include the recovery of four NEOs, improved orbits for additional 76 objects, and the discovery and follow-up of the main-belt asteroid 2004 QR. Two different methods were used to obtain results from photometric observations: Sphere-Cylinder-Plane-element (SCyPe) method is a novel statistical method for fast evaluation of the possible spin and shape spaces for the observed objects and convex inversion has become conventional in solving the inverse problem of obtaining asteroid shapes and their spin characteristics from photometric data. Both of these methods, to date, make use of relatively simple scattering laws, namely Lambert and Lommel-Seeliger laws, instead of more realistic (and subsequently more complex) ones. This is to minimize the number of free parameters and also to optimize the time it takes to compute the solutions. The highlights of the photometric studies with the Nordic NEON are the convex inversion solutions to three asteroids ((1685) Toro, (1981) Midas, and (1862) Apollo) and four new solutions for the possible spin and shape spaces with the SCyPe (for 2002 $FF_{12}$, 2003 $MS_2$, 2003 $RX_7$, and 2004 HW).

## 5.4 Paper IV

**Lunar single-scattering, porosity, and surface-roughness properties with SMART-1/AMIE.** Paper IV presents novel photometric results from the AMIE microimaging camera that acquired in total over 200 000 photometric images of the Moon onboard the ESA SMART-1 lunar mission. For this study, we selected 220 images of lunar maria and of those images we selected only the parts that show little or no albedo variation for the photometric measurements. The broadband filter of AMIE was used since it is currently the best-calibrated channel of the instrument. The data in Paper IV is the first photometric data presented after the new calibration procedures were developed for AMIE (SMART-1 spent large amounts of time inside the Earth's radiation belts and, consequently, the ground calibration images were rendered useles as the camera suffered radiation damage.) They also cover the largest reported phase-angle range in a lunar photometric study from an orbiting platform, to my best knowledge. To study the physical properties of the lunar mare regolith, we utilized novel numerical modelling described in Sect. 2.6. We were able to conclude that the lunar volume-element phase function exhibits a pronounced backscattering-enhancement branch that can be assigned to multiple interactions between single scatterers within the volume element and to the single scatterers themselves. This and the fact that the shadowing mechanisms could not explain well the photometric phase function at phase angles smaller than $\sim 10^\circ$ allowed us to conclude that most of the opposition effect in the lunar maria is caused by coherent backscattering and single scattering within volume elements comparable to lunar particle sizes, with only a small contribution from shadowing effects. This is in stark contrast with the study by Hillier et al. (1999) on Clementine photometry. They explained the opposition effect of mare regions entirely by the shadowing-hiding mechanism ($SM_P$). However, their approach in the analysis of the data was more conventional, utilizing Hapke's scattering law. Another paper, by Shkuratov et al. (1999), utilized data from both Clementine mission

and laboratory measurements together with novel theoretical modelling and reached a conclusion that coherent backscattering could be a major contributor to the lunar opposition effect. In addition, in Paper IV, fBm surface parameters $H = 0.4$ and $\sigma = 0.06$, as well as the packing density of 0.35, were obtained for the lunar maria surfaces.

## 5.5 Paper V

**X-ray fluorescence modelling for solar-system regoliths: Effects of viewing geometry, particle size, and surface roughness.** In Paper V, a foray is made to study the effects of regolith physical properties in soft X-ray energy bands. This study and the ones following it are motivated by the fact that Finland (and more specifically the Department of Astronomy, University of helsinki) is involved in the MIXS/SIXS X-ray spectrometer onboard the future ESA mission to Mercury, BepiColombo (a Finnish Co-PI in MIXS and PI in SIXS). MIXS (Mercury Imaging X-ray Spectrometer) will be the first imaging X-ray spectrometer with focusing optics (i.e., a telescope) to fly to another planet. It will introduce a large improvement in the spectral and spatial capabilities as well as grasp of planetary X-ray spectrometers and thus also pose new challenges to the interpretation of the data, including observation-angle-related effects.

In Paper V, we introduce a new numerical Monte-Carlo ray-tracing code that simulates first-order X-ray fluorescence from a medium that consists of equant spheres of a given elemental composition. We use realistic solar X-ray flux as the input spectrum and limit the study to a medium with a packing density of 0.3. The study is conducted with the angle of incidence at 0°. We study how the particle size and surface roughness affect the measured fluorescent intensity. We note that, as particles become smaller, the observed fluorescent intensity becomes larger. The effect is especially notable at large angles of emergence. Surface roughness introduces a scaling factor to this effect, but if kept constant, does not change the relative significance of the effect between different particle sizes. This implies that, in a medium that is inhomogeneous in composition, i.e., that has particles with different elemental compositions and sizes, the interpretation of measured relative elemental ratios may become unreliable if the angle of emergence is changed between measurements. Also, an opposition effect is seen to arise at $\iota \lesssim 10°$.

## 5.6 Paper VI

**Laboratory studies into the effect of regolith on planetary X-ray fluorescence spectroscopy.** To support the numerical work started in Paper V, a novel experimental setup was designed to study the effects that the physical properties of the regolith have on the soft X-ray fluorescence. These effects are termed the regolith effects in soft X-ray spectroscopy of planetary surfaces in Paper VI, where the experimental work and the results are presented. In addition to the experimental work, a semi-empirical model is presented in this paper for modelling and studying the regolith effects in observed absolute fluorescent elemental line intensities. The experimental setup has been already introduced in Sect.4.2 and further details on the setup are omitted here. Instead of particle size effects, we concentrate on how the surface roughness of the regolith affects the measurements. This is partly because of the necessity of having to press the samples into pellets before they could be measured. The measurements were performed with either the angle of emergence or of incidence fixed at 0°. The other angle could then be moved at an angle-range of $\sim 10 - 50°$. The measured absolute elemental line intensities of Fe and Ca-K$\alpha$ emission are reported as well as the Fe-K$\beta$ as a control measurement. The semi-empirical model was found to describe the angular behaviour of the measured line

intensities accurately. Increased surface roughness was found to harden (enhance the high-energy end) the measured spectra as a function of phase angle (i.e., at all measurement geometries). This result has an impact on, e.g., the interpretation of measurements of relative elemental line intensity ratios from planetary surfaces. Historically, regolith effects have not been accounted for. This can result in overestimation of the concentration of higher Z elements in the measured surface, if the measurements are performed at large phase angles.

## 5.7 Paper VII

**Regolith effects in planetary X-ray fluorescence spectroscopy: Laboratory measurements at 1.7-6.4 keV.** Paper VII continues with the experimental work started in Paper VI. The energy range is extended to include the Si-K$\alpha$ line at 1.74 keV by introducing another experimental setup, MES at the University of Leicester (Sect.4.2). Three samples are used instead of two and the surface characteristics of the samples are better characterized by use of SEM imaging and X-ray tomography. The hypothesis presented in Paper VI, that the particle size distribution of the sample material from which the sample pellet is made of has an effect on the surface roughness of the sample, is confirmed by these imaging techniques. A new way to separate the regolith effects and effects predicted by the fundamental parameters equation (FPE) is presented. It utilizes numerical modelling of FPE with the X-ray source spectrum. Regolith effects are confirmed to introduce hardening of the spectrum at energies down to 1.74 keV, at least for the $\iota = 0^\circ$ geometry, where the measurements were performed.

## 5.8 Author's contribution

My personal contribution to the Papers included in this thesis is as follows. In Paper I, I performed or participated in all of the measurements. I also designed the experimental setup for the parabolic flight campaign and constructed it in collaboration with S. Heikkilä, M. Granvik, and V. Saarinen. Also, I had a leading role in the data reduction and analysis as well as writing the article (as the first author). For Paper II, I performed parts of the measurements and also in wrote parts of the article. In addition, I have been involved in the development of the spectrogoniometers at the Finnish Geodetic Institute, some of which were used in the study reported in Paper II. I performed or participated in all of the photometric observations and most of the astrometric ones at the Nordic Optical Telescope reported in Paper III. I calibrated and reduced all of the photometric images and most of the astrometric ones as well. For this purpose, I wrote a novel Python-IRAF (PyRAF) -based photometry routine and also improved on pre-existing NOTASTROM -routine written for IRAF. I also participated in writing the paper. Paper III has been previously included in the PhD thesis by Torppa (2007). I was responsible for the data calibration for Paper IV. H. Parviainen and I selected the lunar regions imaged by SMART-1/AMIE for this study from a vast dataset of more than 200 000 images utilizing SPICE routines that were partly written by me. Finally, I took part in writing the paper. For Paper V, I continued the development of an X-ray fluorescence simulation code originally written by K. Muinonen. I ran all the X-ray fluorescence simulations and wrote the article, except for Sect. 2.2. I designed the layout of the experimental setup in Paper VI. I participated also in all of the measurements and wrote new software for IDL prgramming language and XSPEC (Arnaud 1996) for data reduction and analysis, which were also performed by me. I wrote all of the paper, except for of Sect. 2. Finally, for Paper VII, I participated in the adjustment of MES for the X-ray fluorescence measurements and took part in all of the

measurements. I calibrated and analyzed the data and the article was written by me.

# 6 Conclusions and future prospects

In the thesis, a variety of methods has been utilized to study how the physical properties of the regolith affect planetary-system research in two distinctly different fields of physics: X-ray fluorescence and VNIR light scattering. Some of the experimental approaches that can be taken to study the opposition effect and BRDF of a particulate sample in visible wavelenghts have been demonstrated. Experimental work at soft X-ray energies has also been carried out to understand the contribution of the regolith effects on the observed fluorescent spectrum. The experimental work is closely linked to more theoretical work. For example, in Paper II, the highly BRDF-dependent behaviour of regoliths is demonstrated, underlining the correctness of the treatment in Paper IV.

In the previous Chapters, it has been shown that the physical characteristics of the regolith can have a significant effect on remote-sensed signal from regolith as a function of measurement geometry. This alteration to the measured signal as compared to a signal expected from an ideal surface is a complex process and largely wavelength dependent. The wavelength also dictates the physical mechanisms that are important in the interaction of electromagnetic radiation and matter. However, in the methodology of the studies of these alteration processes, some similarities appear. In numerical simulations, the main similarities lie in the generation of a realistic medium and in the Monte-Carlo ray-tracing approach taken. Using the same approach to generate, e.g., surface roughness in a medium that is consequently used in studies of different realms of physics, allows us to study what effects do the same physical parameters of the medium have in different wavelengths. With laboratory experiments, as one is dealing with the same kind of sample and also with the same problematics in arranging the goniometric setup and in the data analysis, the multiangular measurements of regolith samples in different wavelengths are perhaps surprisingly similar in nature.

The work started in Paper V shows that the approach used in light-scattering studies can also be extended to other wavelengths. Also, the semiempirical model for soft X-ray fluorescence in Paper VI has its heritage in the Lommel-Seeliger scattering law. The first aim is to tackle the direct problem: "how does particulate nature of regoliths affect the measured signal?" in order to be able to correctly interpret data from planetary missions. However, in the long run also the full-blown inverse problem: "can we obtain physical parameters of the regolith from the data?" can be addressed. In Papers VI and VII, the existence of the regolith effects are experimentally demonstrated and studied. Paper VI is one of the first peer-reviewed journal articles in astronomy to do so.

Prospects for future research in basically all the topics covered by this thesis are bright. As the computational capabilities increase, numerical methods become faster and more complex models for solving the direct and the inverse problem can be incorporated in the analysis of planetary remote-sensed data. New ground-based and space-based instrumentation with better resolution and performance for studying the planetary bodies in the solar system are constantly developed. Their forecoming data will present us with unprecedented opportunities for gaining new knowledge on our solar-system neighbours. However, with these opportunities come also difficulties in understanding the more complex data. As the parameter-space available from data increases, also the models need to be more advanced and more details need to be introduced in calibration and reduction of the data itself. These opportunities and challenges will keep the scientist working in this field occupied for the years to come.

# References


Acton, C. H. (1999), SPICE products available to the planetary science community, *in* 'Lunar and Planetary Institute Conference Abstracts', Vol. 30 of *Lunar and Planetary Institute Conference Abstracts*, p. 1233.

Adler, I. & Trombka, I. J. (1970), *Geochemical exploration of the moon and planets*, Berlin: J. Springer, 1970.

Adler, I., Trombka, J., Gerard, J., Lowman, P., Schmadebeck, R., Blodget, H., Eller, E., Yin, L., Lamothe, R., Gorenstein, P. & Bjorkholm, P. (1972), 'Apollo 15 geochemical X-ray fluorescence experiment: Preliminary report', *Science* **175**, 436–440.

Arai, T., Okada, T., Yamamoto, Y., Ogawa, K., Shirai, K. & Kato, M. (2008), 'Sulfur abundance of asteroid 25143 Itokawa observed by X-ray fluorescence spectrometer onboard Hayabusa', *Earth, Planets, and Space* **60**, 21–31.

Arnaud, K. A. (1996), XSPEC: The first ten years, *in* G. Jacoby & J. Barnes, eds, 'Astronomical Data Analysis Software and Systems V', Vol. 101, Astronomical Society of the Pacific, p. 17.

Bohren, C. & Huffman, D. (1998), *Absorption and scattering of light by small particles*, John Wiley & Sons.

Carpenter, J. (2006), Microchannel plates in astronomy and planetary science, PhD thesis, University of Leicester.

Clark, P. E. & Trombka, J. I. (1997), 'Remote X-ray spectrometry for NEAR and future missions: Modeling and analyzing X-ray production from source to surface', *Journal of Geophysical Research* **102**, 16361–16384.

Courréges-Lacoste, G. B., Schaarsberg, J. G., Sprik, R. & Delwart, S. (2003), 'Modeling of spectralon diffusers for radiometric calibration in remote sensing', *Optical engineering* **41**(12), 3600–3607.

Evans, L. G., Starr, R. D., Brückner, J., Reedy, R. C., Boynton, W. V., Trombka, J. I., Goldstein, J. O., Masarik, J., Nittler, L. R. & McCoy, T. J. (2001), 'Elemental composition from gamma-ray spectroscopy of the NEAR-Shoemaker landing site on 433 Eros', *Meteoritics and Planetary Science* **36**, 1639–1660.

Fairbairn, M. B. (2005), 'Planetary photometry: The Lommel-Seeliger law', *Journal of the Royal Astronomical Society of Canada* **99**, 92–93.

Gehrels, T. (1956), 'Photometric studies of asteroids. V. The light-curve and phase function of 20 Massalia', *Astrophysical Journal* **123**, 331–338.

Glickman, T., ed. (2000), *Glossary of Meteorology*, American Meteorological Society.

Goldsten, J. O., McNutt, Jr., R. L., Gold, R. E., Gary, S. A., Fiore, E., Schneider, S. E., Hayes, J. R., Trombka, J. I., Floyd, S. R., Boynton, W. V., Bailey, S., Brueckner, J., Squyres, S. W., Evans, L. G., Clark, P. E. & Starr, R. (1997), 'The X-ray/gamma-ray spectrometer on the Near Earth Asteroid Rendezvous mission', *Space Science Reviews* **82**, 169–216.

Grande, M., Browning, R., Waltham, N., Parker, D., Dunkin, S. K., Kent, B., Kellett, B., Perry, C. H., Swinyard, B., Perry, A., Feraday, J., Howe, C., McBride, G., Phillips, K., Huovelin, J., Muhli, P., Hakala, P. J., Vilhu, O., Laukkanen, J., Thomas, N., Hughes, D., Alleyne, H., Grady, M., Lundin, R., Barabash, S., Baker, D., Clark, P. E., Murray, C. D., Guest, J., Casanova, I., D'Uston, L. C., Maurice, S., Foing, B., Heather, D. J., Fernandes, V., Muinonen, K., Russell, S. S., Christou, A., Owen, C., Charles, P., Koskinen, H., Kato, M., Sipila, K., Nenonen, S., Holmstrom, M., Bhandari, N., Elphic, R. & Lawrence, D. (2003), 'The D-CIXS X-ray mapping spectrometer on SMART-1', *Planetary and Space Science* **51**, 427–433.

Hapke, B. (1981), 'Bidirectional reflectance spectroscopy. 1. Theory', *Geophysical Research* **86**, 3039–3054.

Hapke, B. (1986), 'Bidirectional reflectance spectroscopy. IV - The extinction coefficient and the opposition effect', *Icarus* **67**, 264–280.

Hapke, B. (1990), 'Coherent backscatter and the radar characteristics of outer planet satellites', *Icarus* **88**, 407–417.

Hapke, B. (1993), *Theory of reflectance and emittance spectroscopy*, Cambridge University Press.

Hapke, B. (2008), 'Bidirectional reflectance spectroscopy. 6. Effects of porosity', *Icarus* **195**, 918–926.

Heiken, G., Vaniman, D. & French, B., eds (1991), *Lunar Sourcebook*, Cambridge University Press.

Hillier, J., Buratti, B. & Hill, K. (1999), 'Multispectral Photometry of the Moon and Absolute Calibration of the Clementine UV/Vis Camera', *Icarus* **141**, 205–225.

Huixian, S., Shuwu, D., Jianfeng, Y., Ji, W. & Jingshan, J. (2005), 'Scientific objectives and payloads of Chang'E-1 lunar satellite', *Journal of Earth System Science* **114**, 789–794.

Huovelin, J., Alha, L., Andersson, H., Andersson, T., Browning, R., Drummond, D., Foing, B., Grande, M., Hämäläinen, K., Laukkanen, J., Lämsä, V., Muinonen, K., Murray, M., Nenonen, S., Salminen, A., Sipilä, H., Taylor, I., Vilhu, O., Waltham, N. & Lopez-Jorkama, M. (2002), 'The SMART-1 X-ray solar monitor (XSM): Calibrations for D-CIXS and independent coronal science', *Planetary and Space Science* **50**, 1345–1353.

Jackson, J. (1999), *Classical Electrodynamics, 3rd edition*, John Wiley & Sons.

Jenkins, R., Gould, R. & Gedcke, D. (1981), *Quantitative X-ray spectrometry*, Marcel Dekker.

Joy, K. H., Crawford, I. A., Kellett, B., Grande, M. N. & the C1XS Science Team (2008), The scientific case for the Chandrayaan-1 X-ray spectrometer, *in* 'Lunar and Planetary Science XXXIX abstracts', p. 1070.

Kaasalainen, S. (2002), Backscattering of light from solar system ices and regoliths, PhD thesis, Observatory, University of Helsinki.

Kaasalainen, S. (2003), 'Laboratory photometry of planetary regolith analogs. I. Effects of grain and packing properties on opposition effect', *Astronomy & Astrophysics* **409**, 765–769.

Kaasalainen, S., Karttunen, H., Piironen, J., Virtanen, J., Liljeström, A. & Näränen, J. (2003), 'Backscattering from snow and ice: laboratory and field measurements', *Canadian Journal of Physics* **81**, 135–143.

Kaasalainen, S., Peltoniemi, J., Näränen, J., Suomalainen, J., Kaasalainen, M. & Stenman, F. (2005), 'Small-angle goniometry for backscattering measurements in the broadband spectrum', *Applied Optics* **44**(8), 1485–1490.

Kaasalainen, S., Piironen, J., Muinonen, K., Karttunen, H. & Peltoniemi, J. (2002), 'Laboratory experiments on backscattering from regolith samples', *Applied Optics* **41**, 4416–4420.

Kreslavsky, M. A., Shkuratov, Y. G., Velikodsky, Y. I., Kaydash, V. G., Stankevich, D. G. & Pieters, C. M. (2000), 'Photometric properties of the lunar surface derived from Clementine observations', *Journal of Geophysical Research* **105**, 20281–20296.

Kuga, Y. & Ishimaru, A. (1984), 'Retroreflectance from a dense distribution of spherical particles', *Journal of the Optical Society of America A* **1**, 831–835.

Lumme, K. & Bowell, E. (1981*a*), 'Radiative transfer in the surfaces of atmosphereless bodies. I - Theory.', *Astronomical Journal* **86**, 1694–1704.

Lumme, K. & Bowell, E. (1981*b*), 'Radiative transfer in the surfaces of atmosphereless bodies. II - Interpretation of phase curves', *Astronomical Journal* **86**, 1705–1721.

Lumme, K. & Irvine, W. (1982), 'Radiative transfer in the surfaces of atmosphereless bodies. III. Interpretation of lunar photometry', *Astronomical Journal* **87**, 1076–1082.

Maruyama, Y., Ogawa, K., Okada, T. & Kato, M. (2008), 'Laboratory measurements of particle size effect in X-ray fluorescence and implications to remote X-ray spectrometry of lunar regolith surface', *Earth, Planets and Space* **60**, 293–297.

Merrill, G. P. (1897), *Rocks, rock-weathering, and soils*, The Macmillan Co.

Mie, G. (1908), 'Beiträge zur Optik trüber Medien, speziell kolloidaler Metallösungen', *Annalen der Physik* **330**, 377–445.

Muinonen, K. (1990), Light scattering by inhomogenous media: Backward enhancement and reversal of polarization, PhD thesis, University of Helsinki.

Muinonen, K., Shkuratov, Y., Ovcharenko, A., Piironen, J., Stankevich, D., Miloslavskaya, O., Kaasalainen, S. & Josset, J.-L. (2002), 'The SMART-1 AMIE experiment: Implication to the lunar opposition effect', *Planetary and Space Science* **50**, 1339–1344.

Nittler, L. R., McCoy, T. J., Clark, P. E., Murphy, M. E., Trombka, J. I. & Jarosewich, E. (2004), 'Bulk element compositions of meteorites: A guide for interpreting remote-sensing geochemical measurements of planets and asteroids', *Antarctic Meteorite Research* **17**, 233–253.

Nittler, L. R., Starr, R. D., Lim, L., McCoy, T. J., Burbine, T. H., Reedy, R. C., Trombka, J. I., Gorenstein, P., Squyres, S. W., Boynton, W. V., McClanahan, T. P., Bhangoo, J. S., Clark, P. E., Murphy, M. E. & Killen, R. (2001), 'X-ray fluorescence measurements of the surface elemental composition of asteroid 433 Eros', *Meteoritics and Planetary Science* **36**, 1673–1695.

Okada, T. (2004), Particle size effect in X-Ray fluorescence at a large phase angle: Importance on elemental analysis of asteroid Eros (433), *in* S. Mackwell & E. Stansbery, eds, 'Lunar and Planetary Institute Conference Abstracts', Vol. 35 of *Lunar and Planetary Institute Conference Abstracts*, p. 1927.

Okada, T., Kato, M., Yamashita, Y., Shirai, K., Yamamoto, Y., Matsuda, T., Tsunemi, H. & Kitamoto, S. (2002), 'Lunar X-ray spectrometer experiment on the SELENE mission', *Advances in Space Research* **30**, 1909–1914.

Okada, T., Shirai, K., Yamamoto, Y., Arai, T., Ogawa, K., Hosono, K. & Kato, M. (2006), 'X-ray fluorescence spectrometry of asteroid Itokawa by Hayabusa', *Science* **312**, 1338–1341.

Ovcharenko, A. A., Bondarenko, S. Y., Zubko, E. S., Shkuratov, Y. G., Videen, G., Nelson, R. M. & Smythe, W. D. (2006), 'Particle size effect on the opposition spike and negative polarization', *Journal of Quantitative Spectroscopy and Radiative Transfer* **101**, 394–403.

Parviainen, H. & Muinonen, K. (2007), 'Rough-surface shadowing of self-affine random rough surfaces', *Journal of Quantitative Spectroscopy and Radiative Transfer* **106**, 398–416.

Peltoniemi, J. I., Kaasalainen, S., Näränen, J., Matikainen, L. & Piironen, J. (2005a), 'Measurement of directional and spectral signatures of light reflectance by snow', *IEEE Transactions on Geoscience and Remote Sensing* **43**, 2294–2304.

Peltoniemi, J. I., Kaasalainen, S., Näränen, J., Rautiainen, M., Stenberg, P., Smolander, H., Smolander, S. & Voipio, P. (2005b), 'BRDF measurement of understory vegetation in pine forests: dwarf shrubs, lichen, and moss', *Remote Sensing of Environment* **94**, 343–354.

Peltoniemi, J. I., Näränen, J., Piironen, J., Kaasalainen, S. & Matikainen, L. (2002), Light scattering by snow, measurements and modeling, *in* 'Third International Workshop on Multiangular Measurements and Modeling', p. 41.

Piironen, J. (1998), Photometry of asteroids at small phase angles with related laboratory measurements, PhD thesis, Observatory, University of Helsinki.

Pinet, P., Cerroni, P., Josset, J.-L., Beauvivre, S., Chevrel, S., Muinonen, K., Langevin, Y., Barucci, M. A., de Sanctis, M. C., Shkuratov, Y., Shevchenko, V., Plancke, P., Hofmann, B. A., Josset, M., Ehrenfreund, P., Sodnik, Z., Koschny, D., Almeida, M. & Foing, B. (2005), 'The advanced Moon micro-imager experiment (AMIE) on SMART-1: Scientific goals and expected results', *Planetary and Space Science* **53**, 1309–1318.

Poehn, C., Wernisch, J. & Hanke, W. (1985), 'Least-squares fits of fundamental parameters for quantitative x-ray analysis as a function of Z ($11 < Z < 83$) and E (1 keV $<$ E $<$ 50 keV)', *X-ray Spectrometry* **14**, 120–124.

Purcell, E. & Pennypacker, C. (1973), 'Scattering and absorption of light by nonspherical dielectric grains', *Astrophysical Journal* **186**, 705–714.

Rayleigh, L. (1871), 'On the light from the sky, its polarization and colour', *Philosophical Magazine* **41**, 107.

Rothery, D., Marinangeli, L., Anand, M., Carpenter, J., Christensen, U., De Santis, M., Epifani, E., Erard, S., Frigeri, A., Fraser, G., Hauber, E., Helbert, J., Hiesinger, H., Joy, K., Langevin, Y., Massironi, M., Milillo, A., Mitrofanov, I., Muinonen, K., Näränen, J., Pauselli, C., Potts, P. & Wurz, P. (2008), 'Mercury's surface and composition studied by BepiColombo', *Planetary and Space Science* **in press**.

Schlemm, C. E., Starr, R. D., Ho, G. C., Bechtold, K. E., Hamilton, S. A., Boldt, J. D., Boynton, W. V., Bradley, W., Fraeman, M. E., Gold, R. E., Goldsten, J. O., Hayes, J. R., Jaskulek, S. E., Rossano, E., Rumpf, R. A., Schaefer, E. D., Strohbehn, K., Shelton, R. G., Thompson, R. E., Trombka, J. I. & Williams, B. D. (2007), 'The X-Ray Spectrometer on the MESSENGER Spacecraft', *Space Science Reviews* pp. 393–415.

Schulz, R. & Benkhoff, J. (2006), 'BepiColombo: Payload and mission updates', *Advances in Space Research* **38**, 572–577.

Shiraiwa, T. & Fujino, N. (1966), 'Theoretical Calculation of Fluorescent X-Ray Intensities in Fluorescent X-Ray Spectrochemical Analysis.', *Japanese Journal of Applied Physics* **5**, 886–899.

Shkuratov, Y. G. (1988), 'A diffraction mechanism for the formation of the opposition effect of the brightness of surfaces having a complex structure', *Kinematika i Fizika Nebesnykh Tel* **4**, 33–39.

Shkuratov, Y. G., Kreslavsky, M. A., Ovcharenko, A. A., Stankevich, D. G., Zubko, E. S., Pieters, C. & Arnold, G. (1999), 'Opposition effect from Clementine data and mechanisms of backscatter', *Icarus* **141**, 132–155.

Shkuratov, Y. G., Stankevich, D. G., Petrov, D. V., Pinet, P. C., Cord, A. M., Daydou, Y. H. & Chevrel, S. D. (2005), 'Interpreting photometry of regolith-like surfaces with different topographies: shadowing and multiple scattering', *Icarus* **173**, 3–15.

Stankevich, D., Shkuratov, Y., Grynko, Y. & Muinonen, K. (2003), 'Computer simulations for multiple scattering of light rays in systems of opaque particles', *Journal of Quantitative Spectroscopy and Radiative Transfer* **76**, 1–16.

Tertian, R. & Claisse, F. (1982), *Principles of quantitative X-ray fluorescence analysis*, Heyden.

Torppa, J. (2007), Lightcurve inversion for asteroid spins and shapes, PhD thesis, University of Helsinki.

van de Hulst, H. C. (1957), *Light scattering by small particles*, John Wiley & Sons.

van de Hulst, H. C. (1970), 'The Spectrum of the Anisotropic Transfer Equation', *Astronomy and Astrophysics* **9**, 366–373.

Van Grieken, R. & Markowicz, A., eds (2002), *Handbook of X-ray Spectrometry, 2nd. edition*, Marcel Dekker.